Journal of
Medicinal
Chemistry

pubs.acs.org/jmc

Article

Discovery of a Potent and Selective Tyrosine Kinase 2 Inhibitor: TAK-279

Silvana Leit, Jeremy Greenwood, Samantha Carriero, Sayan Mondal, Robert Abel, Mark Ashwell, Heather Blanchette, Nicholas A. Boyles, Mark Cartwright, Alan Collis, Shulu Feng, Phani Ghanakota, Geraldine C. Harriman, Vinayak Hosagrahara, Neelu Kaila, Rosanna Kapeller, Salma B. Rafi, Donna L. Romero, Paul M. Tarantino, Jignesh Timaniya, Angela V. Toms, Ronald T. Wester, William Westlin, Bhaskar Srivastava, Wenyan Miao, Peter Tummino, Joshua J. McElwee, Scott D. Edmondson,* and Craig E. Masse

Cite This: *J. Med. Chem.* 2023, 66, 10473−10496

Read Online

ACCESS | Metrics & More | Article Recommendations | Supporting Information

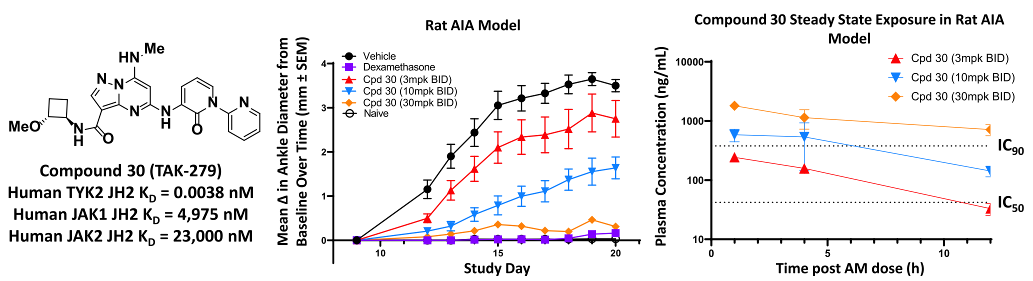

ABSTRACT: TYK2 is a key mediator of IL12, IL23, and type I interferon signaling, and these cytokines have been implicated in the pathogenesis of multiple inflammatory and autoimmune diseases such as psoriasis, rheumatoid arthritis, lupus, and inflammatory bowel diseases. Supported by compelling data from human genome-wide association studies and clinical results, TYK2 inhibition through small molecules is an attractive therapeutic strategy to treat these diseases. Herein, we report the discovery of a series of highly selective pseudokinase (Janus homology 2, JH2) domain inhibitors of TYK2 enzymatic activity. A computationally enabled design strategy, including the use of FEP+, was instrumental in identifying a pyrazolo-pyrimidine core. We highlight the utility of computational physics-based predictions used to optimize this series of molecules to identify the development candidate **30**, a potent, exquisitely selective cellular TYK2 inhibitor that is currently in Phase 2 clinical trials for the treatment of psoriasis and psoriatic arthritis.

■ INTRODUCTION

Tyrosine kinase 2 (TYK2) is a highly validated therapeutic target being pursued for the treatment of autoimmune and inflammatory diseases.[1−3] TYK2 propagates the downstream intracellular signaling of the pro-inflammatory cytokines IL12, IL23, and type I interferon. These cytokines each play a critical role in the function of Th1 and Th17 cells and consequently play a key role in a range of autoimmune and chronic inflammatory diseases. Genome-wide association studies have identified loss-of-function (LoF) mutations of TYK2 in humans, which have been shown to be protective for a number of inflammatory diseases.[4−7] These LoF variants reduce the function of TYK2 to mediate cytokine signaling, which in turn confers protection against a number of diseases.[6,8−10] Importantly, analysis of data from subjects carrying the rs34536443 single nucleotide polymorphism (SNP) revealed a greater level of protection conferred by homozygous mutations compared to heterozygous mutations.[6] The homozygous C/C mutation affords more than double the protective effect as the heterozygous C/G mutant against ankylosing spondylitis, Crohn's disease, multiple sclerosis, psoriasis, and ulcerative colitis. Moreover, for ulcerative colitis, only the homozygotes were protected. The rs34536443 SNP codes for a substitution of a proline residue with an alanine residue in the kinase domain of TYK (P1104A) and homozygote SNP mutations result in a greater reduction in the catalytic function of TYK2 than heterozygous mutations. This observation suggests that higher levels of inhibition of TYK2 through a small molecule inhibitor may confer improved efficacy compared to patients in whom TYK2 is inhibited to a

Received: April 3, 2023
Published: July 10, 2023

ACS Publications

© 2023 American Chemical Society

https://doi.org/10.1021/acs.jmedchem.3c00600

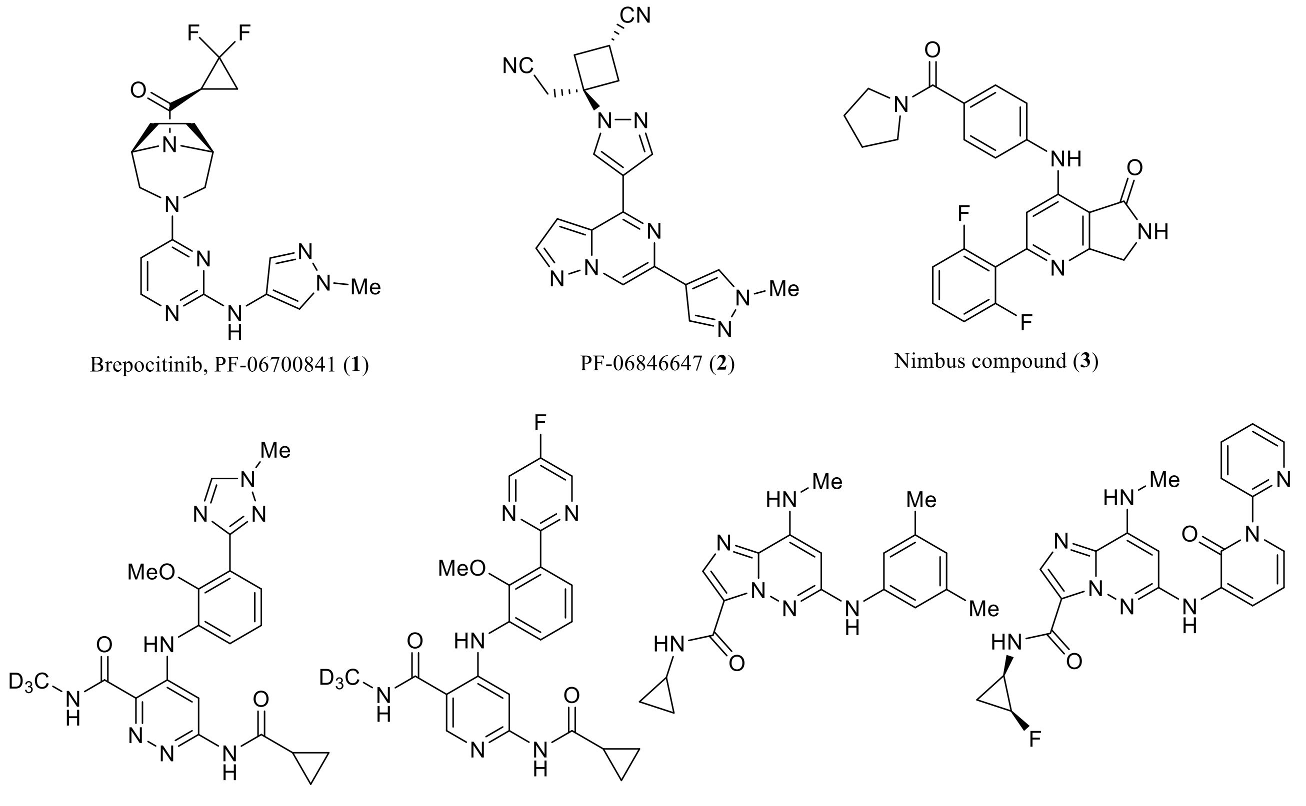
Brepocitinib, PF-06700841 (**1**)
PF-06846647 (**2**)
Nimbus compound (**3**)
Deucravacitinib, BMS-986165 (**4**)
BMS-986202 (**5**)
BMS Compound (**6a**)
BMS Compound (**6b**)

Figure 1. Selected small molecule JH1 TYK2 inhibitors, including: brepocitinib (**1**), ropsacitinib (**2**), Nimbus compound **3**, and JH2 TYK2 inhibitors, including: deucravacitinib (**4**), BMS-986202 (**5**), and BMS compounds **6a** and **6b**.

lesser degree. Finally, in a separate genetic study examining over 30,000 subjects with linked electronic medical records, no adverse effects of the P1104A variant were noted.[5] Inhibitors of TYK2 are currently in clinical development and have shown efficacy in psoriasis, psoriatic arthritis, and systemic lupus erythematosus.[11−16] Given its robust genetic, biological, and clinical validation, TYK2 inhibition has attracted significant attention in the pharmaceutical industry in recent years.[17−19]

TYK2 is a member of the Janus kinase (JAK) family of kinases, which includes JAK1, JAK2, and JAK3. Members of the JAK kinase family regulate signals from multiple cytokine receptors, as well as from growth hormone and erythropoietin. A range of adverse effects are associated with inhibition of JAK1, JAK2, and/or JAK3.[20−22] Therefore, high selectivity for TYK2 over those isoforms is needed to achieve high levels of in vivo TYK2 inhibition without the risk of these adverse effects. The orthosteric (catalytic) binding pocket of TYK2, also known as the Janus homology 1 (JH1) domain, possesses a high degree of homology to the JH1 domain of other members of the JAK family. This high homology between the JH1 binding sites makes selective inhibition of TYK2 over other JAKs very challenging to achieve.[23] Two clinical-stage TYK2 inhibitors, brepocitinib (PF-06700841, **1**),[24] and ropsacitinib (PF-06826647, **2**),[25] are JH1 inhibitors of TYK2 and we have recently reported our own research of the discovery of the novel JH1 TYK2 inhibitor compound **3** (Figure 1).[26] More recently, inhibition of TYK2 through the allosteric pseudokinase domain, also known as the Janus homology 2 (JH2) domain, has been reported. Deucravacitinib (BMS-986165, **4**)[27] is the first drug in this new class of TYK2 inhibitors that was recently approved by the FDA. Additionally, BMS-986202 (**5**)[28] was reported to be a clinical-stage compound that inhibits TYK2 through the JH2 binding site. An early report on a series of imidazopyridazines represented by compound **6a**[29] first demonstrated the selectivity of these JH2 inhibitors compared to the JH1 inhibitors. Table 1 compares the inhibitory potency of the previously reported TYK2 inhibitors **1−6** against the JAK family JH1 domain. The TYK2 JH2 inhibitors **4−6** exhibit higher selectivity for TYK2 over JAK1, JAK2, and JAK3 compared to the TYK2 JH1

Table 1. Reported TYK2 Inhibitors and Their Respective JAK Family Biochemical Activity[a]

	Assay IC_{50} or *Ki* (nM)			
Compound	JAK1 (JH1)	JAK2 (JH1)	JAK3 (JH1)	TYK2 (JH1/JH2)
1[b]	17	77	6494	23/nd
2[b]	383	74	>10,000	17/nd
3[c]	46	22	6.6	0.51/nd
4[d]	>10,000	>10,000	>10,000	>10,000/0.2
5[d]	>10,000	>10,000	>10,000	>10,000/0.19
6a[e]	>10,000	>10,000	>10,000	>10,000/0.13
6b[e]	>10,000	>10,000	>10,000	>10,000/0.086

[a] nd = not determined. [b] Assays to determine IC_{50}s were run in the presence of 1 mM of ATP according to ref 24 for **1** and ref 25 for **2**. [c] Assays to determine the K_i values for **3** were run in the presence of 10 μM of ATP, according to ref 26. [d] Assays used homogeneous time-resolved fluorescence (HTRF) binding assay formats to measure the displacement of a probe compound to the JH2 domain, as reported in ref 27 for **4** and ref 28 for **5**. [e] Assays to determine the K_i of the JH1 domains were run in the presence of 10 μM of ATP according to ref 26, and the K_i values of the TYK2 JH2 domain were reported in ref 37 for **6a** and **6b**.

Downloaded from https://papernode.pages.dev

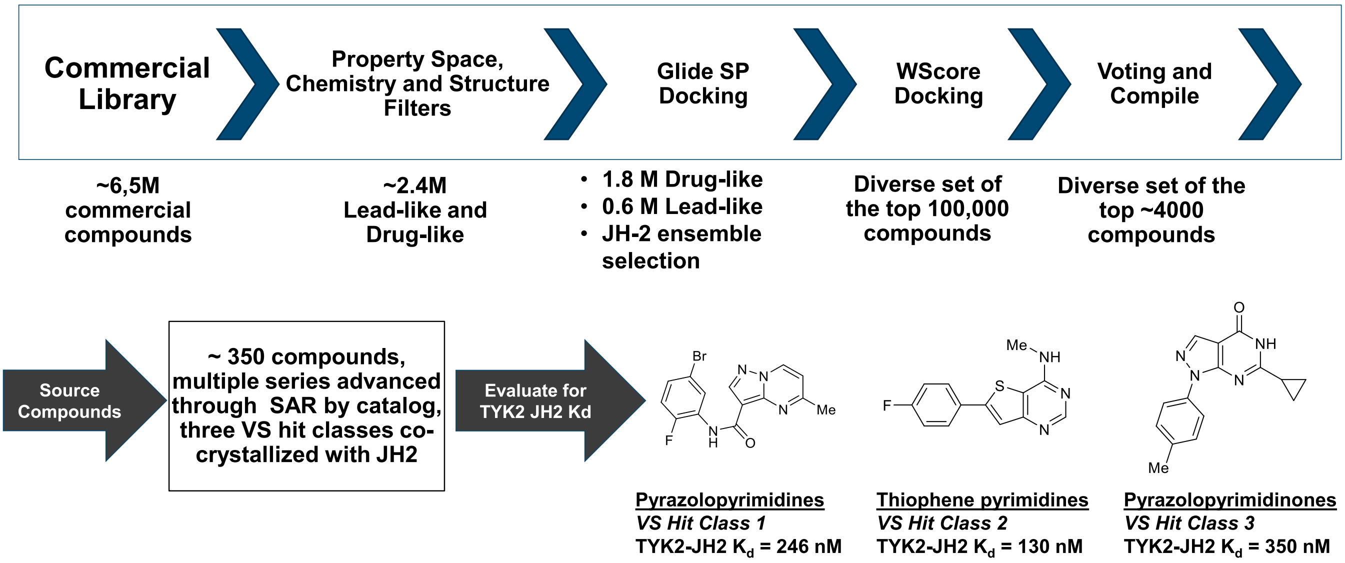

Figure 2. Virtual Screen triage scheme to identify three novel hit classes for the TYK2 JH2 domain.

inhibitors **1**−**3**. We thus focused our TYK2 inhibitor drug discovery efforts on the JH2 domain for TYK2 inhibition, as this approach has demonstrated that high levels of selective TYK2 inhibition can be achieved in the clinic without the risk of adverse effects due to off-target inhibition of JAK1-3.

At the outset of this work, we leveraged X-ray co-crystal structures reported for compounds bound to the JH2 domain of TYK2 for a structure-based virtual screen (VS) of a large database of commercially available compounds. To limit the screen to lead-like and drug-like compounds, a library of ∼6.5 million commercially available compounds was first narrowed to about 2.4 million compounds by structure filter restriction of property space (see Supporting Information for details). This smaller library was next assessed in a virtual screen (VS) with a JH2 ensemble structural selection developed from reported X-ray crystal structures from PDB ID codes[29] 4WOV,[30] 5C01,[31] 5C03,[31] and 3Z0N[32] using the Glide SP docking program[33] with a hinge constraint. Next, a diverse set of the top ∼100,000 compounds was assessed using WScore docking for a more accurate treatment of water molecules in the binding pocket.[34] The WScore triage results were compiled, and a voting system was used to rank a structurally diverse set of the top ∼3500 compounds. We then sourced ∼340 compounds and measured their respective TYK2 JH2 domain binding potencies. Promising hits were progressed through SAR by catalog to identify similar neighbors. Ultimately, 3 structurally distinct hit classes were identified, including a pyrazolopyrimidine class, a thiophene−pyrimidine class, and a pyrazolopyrimidinone class (Figure 2). Although all three of these classes were promising leads, we were especially intrigued by the steric and electronic similarity between the pyrazolopyrimidine core heterocycle and the imidazopyridazine core of compound **6a**.

To follow-up on the possibility of incorporating a scaffold-hop strategy to replace the imidazopyridazine ring of **6a** with a pyrazolopyrimidine core similar to the core identified in VS hit class 1 from Figure 2, we applied the physics-based computationally guided structure-based drug design (SBDD) tool free energy perturbation (FEP+) to guide compound design in this scaffold-hop series.[35] We used FEP+ to compute the binding potency of designed ligands for the JH2 and JH1 binding sites of TYK2, taking into account the entropic and enthalpic effects of ligands in solvent and in protein, as well as the local dynamics of protein residues and second-shell effects. FEP+ was run with the OPLS3 forcefield. Cycle closure was employed before any synthesis prioritization, and the potency of a new idea was computed via multiple different perturbation paths to ensure consistent results among the different perturbation paths. Calculations were run for simulation time >10 ns per lambda window, and extended as needed for convergence. The integration of FEP+ modeling and medicinal chemistry ideation allowed us to focus the synthetic effort on the highest-priority target molecules. Importantly, this approach allows for the early elimination of those ideas that are unlikely to meet the desired affinity of JAK family selectivity thresholds. This manuscript will describe the optimization of these pyrazolopyrimidines (Figure 3) to deliver a potent and highly selective TYK2 inhibitor that binds to the JH2 domain.

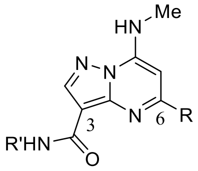

Figure 3. General structure of pyrazolopyrimidine TYK2 inhibitors.

■ RESULTS AND DISCUSSION

To prioritize a designed compound for chemical synthesis, we first assessed binding potencies to the JH2 domain of TYK2 through the in silico use of FEP+. For these calculations, we used the same protein domain construct as was used for the TYK2 JH2 binding assay—a displacement probe assay (DiscoveRx) with the JH2 pseudokinase domain (amino acids G556 to D888). Correlations between predicted and measured binding affinities for the new pyrazolopyrimidine series were sufficiently accurate for use as a key triage element for compound synthesis (e.g., 96% of the predicted potencies were within 100-fold of the measured potencies, and the overall mean absolute error (MAE) was 0.7 log order, Figure 4). Specifically, the calculated potencies using FEP+ were used to help focus chemistry on compounds with binding affinities in the picomolar range for K_D

Downloaded from https://papernode.pages.dev

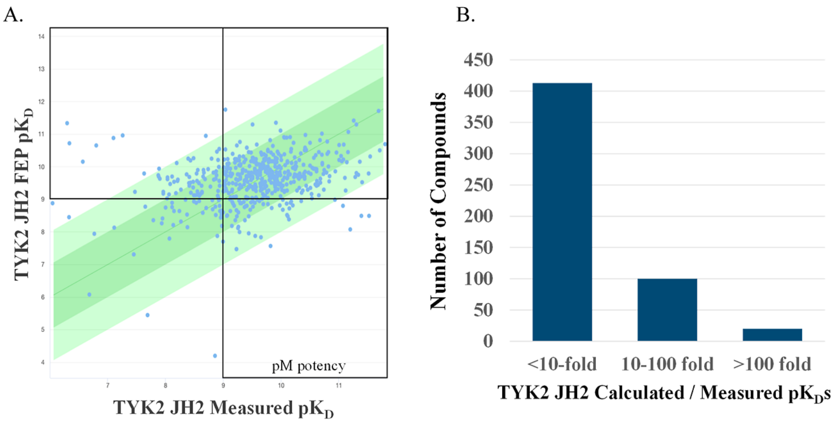

Figure 4. Prospective potency predictions using FEP+ for the TYK2 JH2 binding domain in the pyrazolopyrimidine series. (A) Scatter plot showing predicted TYK2 JH2 potencies (*y*-axis) and measured TYK2 JH2 potencies (*x*-axis) for compounds that were synthesized. Compounds in the dark green region are within 10-fold, and those in the lighter green region are within 100-fold of their measured potencies. (B) Bar graph showing pyrazolopyrimidines assessed in FEP+ prior to synthesis. Of 533 compounds assessed, 413 (77%) were predicted within 10-fold and 513 (96%) were predicted within 100-fold of the measured potency. The overall MAE is 0.7 log-order.

Table 2. Scaffold-Hopping to a Pyrazolo-Pyrimidine Series[a]

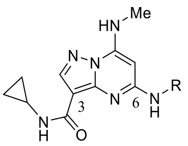

Compound	R	ALogP[a]	TYK2 JH2 FEP+ K_D (nM)	TYK2-JH2 K_D[b] (nM)	PDE4D IC_{50}[b] (nM)	PBMC pSTAT4 IL12 IC_{50}[b] (nM)	Kin Sol pH 7.4[b] (μM)
7	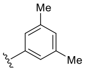 Me Me	3.0	--	0.078[c]	36	14	<0.1[c]
8	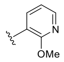 N OMe	1.8	0.13	0.039[c]	250	26	5.5
9	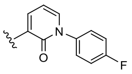 N O F	2.7	0.050	0.063[c]	>10,000	45	0.15
10	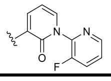 N N O F	2.1	0.40	0.099[c]	--	21	7.3

[a] All compounds exhibit >30,000 nM binding K_Ds to the JH1 binding domains of JAK1, JAK2, JAK3, and TYK2 [b] A log *P* calculated, as described in ref 40. [c] Unless otherwise noted, each assay run was performed with *n* = 1. [d] Value is the average of *n* ≥ 2 assay runs.

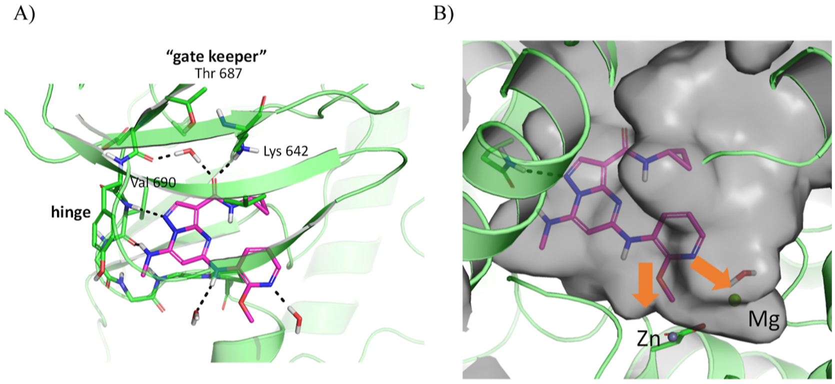

Figure 5. (A) X-ray co-crystal structure of compound **8** bound to the JH2 domain of TYK2 at 1.87 Å (PDB: 8S98). (B) Model of compound **8** bound to PDE4D (based on PDB 5TKB).[29]

values (see Supporting Information for a histogram of predicted potency for a R-group scan as an illustration). With 96% of the calculated binding affinities of compounds in Figure 4 falling within 100-fold of their measured binding potencies and 77% within 10-fold of the predicted potencies, the calculated potencies helped render a "Go/No Go" decision for the

Downloaded from https://papernode.pages.dev

Table 3. SAR for a Series of Amides

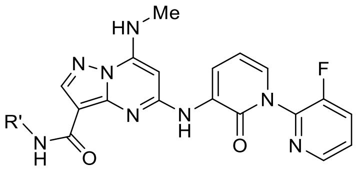

Compound	R'	ALogP[a]	TYK2-JH2 K_D[b] (nM)	hPPB Fu[b] (%)	PBMC IL12 / pSTAT4 IC_{50}[b] (nM)	Kin Sol pH 7.4[b] (μM)
11		2.0	0.068[c]	9.9	22[c]	31
12	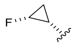	2.0	0.073[c]	3.8	68	7.3
13	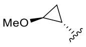	1.7	0.023	12	58	27
14		1.7	0.088	15	>50[d]	36
15	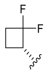	2.7	0.0077[c]	6.6	9.0	0.6
16	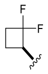	2.7	0.31[c]	3.7	--	0.6
17	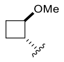	2.1	0.0031[c]	22	6.8	14
18	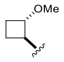	2.1	0.20	19	--	18
19[e]	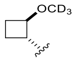	2.1	0.0030[c]	19	13	10
20	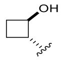	1.5	0.0076[c]	22	>50	22
21	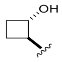	1.5	0.13	28	320[c]	41
22	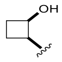	1.5	0.019	22	>50[d]	79
23	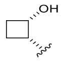	1.5	0.48	17	--	100
24	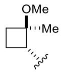	2.5	0.086[c]	16	>50[d]	304
25	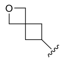	2.1	0.46[c]	26	>50[d]	5.6
26	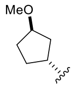	2.5	0.38[c]	18	--	26
27	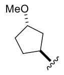	2.5	2.7[c]	16	--	--
28		1.7	0.033[c]	23	170	22

[a] A log *P* calculated, as described in ref 40. [b] Unless otherwise noted, each assay run was performed with $n = 1$. [c] Value is the average of $n \geq 2$ assay runs. [d] Percent inhibition was <50% when tested at a single concentration of 50 nM. [e] Most potent enantiomer shown.

synthesis of a compound. This strategy was particularly useful in the earlier stages of the optimization process when new core(s) were assessed in combination with the large array of substituents reported in patents or published TYK2 literature, where potencies were not always in the sub-nanomolar range. The FEP+ potency predictions helped keep the project team focused on the most potent TYK2 JH2 binding ligands.

Among the most potent of a range of scaffold-hop concepts that were assessed was compound **7**, a pyrazolopyrimidine scaffold replacement analog[36] of compound **6a** (Table 2). In addition to its potent binding to the TYK2 JH2 domain, compound **7** also exhibited good TYK2 cellular activity (IC_{50} = 14 nM), measured by inhibition of phosphorylation of STAT4 in an IL12-stimulated primary human peripheral blood mononuclear cell (PBMC) assay. Pyrazolopyrimidine **7** suffered from off-target activity against PDE4D, as reported previously for compound **6a**.[29] When the dimethylphenyl group was replaced with a methoxypyridine (compound **8**), the high JH2 TYK2 binding potency and PBMC pSTAT4 cell potency were retained, while the PDE4D selectivity improved. Perhaps not surprisingly, the more lipophilic compound **7** exhibited poor kinetic solubility (<0.1 μM at pH 7.4), while pyridine **8** exhibited modest but nevertheless improved solubility. An X-ray co-crystal structure of **8** bound to the JH2 domain of TYK2 shows key interactions of the pyrazolopyrimidine hit series with the pseudokinase domain of the protein (Figure 5). Key

https://doi.org/10.1021/acs.jmedchem.3c00600
J. Med. Chem. 2023, 66, 10473−10496

Downloaded from https://papernode.pages.dev

Table 4. Cellular and Whole Blood Potencies, Permeabilities, and Hepatocyte Clearance for a Selected Series of TYK2 Inhibitors

Compound	PBMC GM-CSF/pSTAT5 IC$_{50}$ (nM)[a]	PBMC IL2/pSTAT5 IC$_{50}$ (nM)[a]	Hum/Mur WB IFNα/CXCL10 IC$_{50}$ (nM)[a]	Caco-2 P_{app}[a] A−B/ER	Hum/Rat Hep[a] CL$_{pred}$ (mL/min/kg)
11	>50,000[b]	>50,000	330[b]/2640[b]	15/1.3	1.8/20
13				4.1/4.7	<LoQ[c]/30
15					4.8/21
17	>50,000	>50,000	43/372	10/2.2	2.3/25
19					2.0/32
20				3.0/5.1	6.7/8.7
30	>50,000[b]	>50,000[b]	22[b]/347[b]	15/1.0	0.69[d]/30
34	>50,000	>50,000	56/254	6.1/4.4	1.7/
39	>20,000	>20,000		3.4/7.6	<LoQ[c]/38

[a] Unless otherwise noted, each assay run was performed with $n = 1$. [b] Value is the average of $n \geq 2$ assay runs. [c] <LoQ = below the limits of quantification in the assay (no detectable turnover). [d] Hepatopac low turnover assay.

interactions include the hinge binding region with the pyrazole ring, the methylamine substituent, and Val690 of TYK2. Additionally, the unique DPG moiety of the pseudokinase domain impacts the position of the conserved pseudo-catalytic Lys642,[30] such that it forms a hydrogen bond with the carbonyl group of **8**. The crystal structure suggests that larger substituents projecting from the pyridine ring (toward the Zn binding region) would likely be tolerated for TYK2 potency but not for PDE4D potency (Figure 5). Supported by promising FEP+ predicted TYK2 JH2 potencies, we explored a series of N-aryl pyridines, as the larger aromatic rings were predicted to retain potency for binding TYK2 while further improving selectivity over PDE4D. This pyridone series, exemplified by compounds **9** and **10**[36] afforded a different vector from which to build substituents which were likely to retain TYK2 potency while minimizing PDE4D inhibitory activity by projecting toward the Mg binding region of this protein (Figure 4). Both **9** and **10** proved to be potent TYK2 JH2 binders, and both retained a high level of PBMC pSTAT4 cellular potency. The less lipophilic compound **10** exhibited moderately improved solubility compared to the fluorophenyl analog **9**. As anticipated based on our PDE4D docking analyses, compound **9** was highly selective over PDE4D (IC$_{50}$ > 10,000 nM). In parallel to our work in this series, the SAR of a series of N-aryl pyridones was reported with structurally similar imidazopyridines such as compound **6b**.[37] The use of calculated (FEP+) potencies to prioritize compound synthesis for these C6 substituents proved effective in narrowing our focus to the most potent substituents. Accordingly, the FEP+ calculated potencies are shown alongside the measured TYK2 JH2 binding potencies for compounds **8**−**10** in Table 2 and the measured binding potencies were all within ∼5-fold of their calculated potencies. Additionally, as expected based on their JH2 binding modes, all four of the potent TYK2 inhibitors **7** through **10** exhibited K_i values > 10,000 nM against the JH1 domains of JAK1, JAK2, JAK3, and TYK2. Furthermore, compounds **7**−**10** were each assessed in human cellular assays reflective of off-target inhibition of JAK2 (human PBMCs, GM-CSF-induced pSTAT5)[38] as well as JAK1 and JAK3 (human PBMCs, IL2-induced pSTAT5).[39] All four compounds displayed high levels of functional cellular selectivity in the PBMC assays (IC$_{50}$s > 50,000 nM), further underscoring the pyrazolopyrimidine series as a promising starting point for further optimization.

The rank order of pSTAT4 cellular potencies for the compounds in Table 2 is somewhat disconnected from the corresponding rank order TYK2 JH2 binding potencies. The potency disconnects between biochemical TYK2 inhibition and cellular activity have been observed in previous reports of TYK2 JH2 inhibitors.[29,39] We also note the drop in potency in the PBMC assay, which can be due to a number of possible factors, including the presence of physiologically relevant cellular ATP concentrations, the protein binding to the 10% fetal calf serum in the assay medium, differences in binding between the full-length protein in cells compared to the recombinant JH2 domain protein, and the possibility that the binding potencies of these compounds may be nearing the lower limit of the dynamic range of the JH2 binding assay. These differences result in a loss of resolution in the compound potency rank order.

With the discovery of this new series of potent and selective TYK2 inhibitors and the ability to use FEP+ to identify compounds with a high level of binding potency to the TYK2 JH2 domain, we also sought to design compounds with good drug-like properties. The kinetic solubilities for compounds in Table 2 are low, indicating a potential challenge with oral absorption. To address this challenge, we implemented a predictive RRCK model for passive permeability[41] in conjunction with a predictive FEP+ solubility model.[42] We recognized that optimization of kinetic solubility with these neutral molecules might be difficult, so it was important to ensure that they maintained good permeability in addition to adequate solubility to ensure high oral absorption. To improve solubility, we retained the fluoropyridyl-pyridone while exploring amide replacements for the cyclopropane ring (Table 3). The X-ray co-crystal structure of **8** bound to the TYK2 JH2 domain, and consequently the FEP+ predicted potencies, suggested that more sterically demanding amides may not be well tolerated for TYK2 JH2. Consequently, amides such as **27**−**29** exhibited significantly reduced binding affinity to TYK2. In general, cyclobutyl and cyclopropyl amides were well tolerated, although there appeared to be a preferred stereochemical configuration for high affinity binding to TYK2, as stereoisomers **14**, **16**, **20**, **23**, **25**, and **26** are all suboptimal binders to TYK2 compared to their antipodes. Potent but lipophilic fluorinated cyclopropyl and cyclobutyl amides, such as **12** and **15**, exhibited kinetic solubilities less than 10 μM, which were insufficient for compound progression. An exception was **11**, which exhibited moderate kinetic solubility (31 μM) and thus was an improvement over **10**, **12**, and **15**. We observed a significant potency enhancement in binding to the JH2 domain of TYK2 for a series of “privileged” cyclobutyl amides with defined stereochemistry (vide supra), and the introduction of more polar methoxy or hydroxy substituents to the cyclobutane ring system contributed to some improved kinetic solubilities for this subseries. One particularly relevant set of enantiomers is **17**

Downloaded from https://papernode.pages.dev

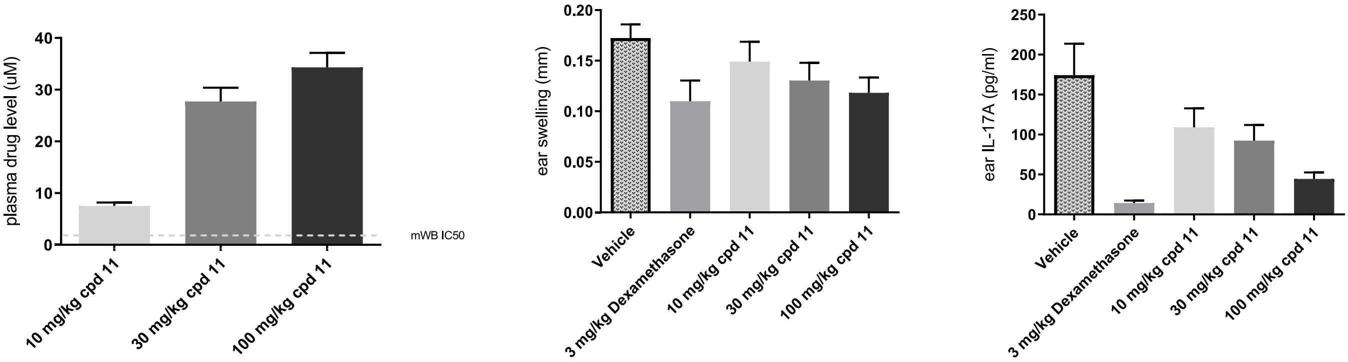

Figure 6. Profile of **11** in a mouse IL23-induced ear swelling psoriasis model with dexamethasone (3 mg/kg) used as a positive control. (A) Mouse pharmacokinetic profile at 1 h post last dose of **11** at oral doses of 10, 30, and 100 mg/kg BID relative to the mouse whole blood IFNα-IP10 IC$_{50}$. (B) Dose-dependent reduction of ear swelling observed with **11** in the IL23-induced inflammation model. (C) Dose-dependent reduction of IL17A was measured in the IL23-induced mouse inflammation model. The 100 mg/kg dose was comparable to dexamethasone in this model.

and **18**, which possess a ~65-fold difference in binding potency to the TYK2 JH2 domain. The more potent enantiomer is the *R,R* configuration, as depicted in Table 3. Assessment of PBMC pSTAT4 cellular potencies of selected compounds revealed a general correlation of cell potencies with TYK JH2 binding potencies with few exceptions. Two exceptions include compounds **13** and **28**, which were less potent in the cell assay than anticipated based on their TYK2 JH2 binding potencies. All compounds in Table 3 exhibit low binding affinity (K_Ds > 10,000 nM) to the JH1 binding domains of JAK1, JAK2, JAK3, and TYK2.

We further assessed a sub-series of compounds from Table 3 with IL12-induced pSTAT4 PBMC potencies less than 100 nM in a second tier of cellular assays to further assess JAK family selectivity and in vitro ADME assays to better determine which may be amenable to further evaluation (Table 4). Similar to **7**–**10**, compounds **11**, **17**, and **28** exhibited no activity even at the highest concentrations measured in the GM-CSF and IL2 pSTAT5 assays described above, indicating that they do not block signaling through JAK1, JAK2, or JAK3. We also assessed **11** and **17** for inhibition of IFNα-induced cytokine (CXCL10) production in human and mouse whole blood (WB).[39] We observed additional potency shifts for these two compounds in the WB assay compared to their PBMC pSTAT4 assay potencies, which we attribute to plasma protein binding. Compounds **11**, **13**, **17**, and **19** all possessed excellent stability in human hepatocytes, while **15** and **20** both exhibited suboptimal human hepatocyte stability. Unfortunately, the more polar analogs **13** and **20** each possessed increased efflux ratios in the Caco-2 assay, suggesting a risk for suboptimal oral absorption. Incorporation of a tri-deuteromethoxy group into **19** resulted in only a modest improvement in human hepatocyte stability relative to the corresponding methyl analog **17** with similar potency in the PBMC IL12 pSTAT4 cellular assay (within approximately 2-fold).

Compound **11** was an early lead in this series and was selected for additional characterization. The overall in vitro selectivity profile of **11** was excellent. It exhibited a high level of selectivity against PDE4D and hERG (IC$_{50}$s > 10 and 30 μM, respectively) as well as IC$_{50}$s > 30 μM against human CYP3A4 (midazolam and testosterone), CYP2D6, CYP2C9, CYP2C19, and CYP1A2. Evaluation of **11** at 1 μM in a panel of 611 kinases (10 μM ATP concentration) revealed a clean overall kinome selectivity profile. Apart from TYK2, less than 50% inhibition was observed for all but four kinases: c-Kit (63% inhibition), c-MET (54% inhibition), HIKP4 (52% inhibition), and EGFR (51% inhibition). The in vivo pharmacokinetic profile of **11** in mice, rats, dogs, and cynomolgus monkeys is summarized in Table 6. Its low clearance and relatively flat (low peak-to-trough) in vivo oral PK profile in mice suggested that this compound might serve as an ideal rodent tool compound for an in vivo PD study. Consequently, we evaluated **11** in a mouse IL23-induced epidermal hyperplasia model (Figure 6).[43] IL23 was injected into the ear of C57BL/6 mice on day 0. IL23, in turn, induces IL17 by dermal $\gamma\Delta$ T cells and leads to the production of inflammatory cytokines. These cytokines induce immune cell infiltration, keratinocyte proliferation, and epidermal hyperplasia, resulting in skin redness and thickening. Compound **11** reduced inflammation induced by IL23 in the mouse and elicited a dose-dependent reduction of IL17A in the ear. The 100 mg/kg BID group saw a maximum reduction of 75% relative to the vehicle-treated group. The efficacy (reduction of ear swelling) at this dose was comparable to the efficacy observed in the dexamethasone treated mice. Plasma samples from 1 h (T_{max}) post dose were evaluated to confirm exposure. While all doses showed exposures that exceeded the mouse IFNα induced CXCL10 IC$_{50}$, only the 100 mpk BID dose was predicted to provide 24 h coverage. This data suggests that a trough level that exceeds the whole blood IFNα IC$_{50}$ is needed for good efficacy in this model, consistent with a previous report in a different mouse model.[39]

Using the human WB IFNα IC$_{50}$ as a target trough coverage, we next performed a human dose prediction for **11**. The in vitro–in vivo extrapolation (IVIVE) of **11** across mice, rats, dogs, and cynomolgus monkeys suggested a good overall correlation between hepatocyte stability and in vivo clearance, indicating that human hepatocyte stability should be predictive of human clearance. Using allometric and IVIVE modeling, predictions of human clearance ranged from 3.7 to 7.2 mL/min/kg at steady state, with a predicted volume of ≤1.0 L/kg and approximately 50% bioavailability. Accordingly, a BID dose of 200 mg, or a QD dose ≥1 g, may be required to afford continuous coverage of the human WB IC$_{50}$. This predicted human dose range was too high to warrant further progression of **11**, and therefore our focus shifted to improving human hepatocyte stability as well as the potency of human WB to optimize the predicted human dose. Given the human genetic data suggesting that greater TYK2 inhibition might translate to improved efficacy in humans, we sought to identify a compound with a significantly lower human dose prediction than **11**.

Downloaded from https://papernode.pages.dev

To better understand the key interactions with this promising aryl-pyridone sub-series, we generated a co-crystal structure of the TYK2 JH2 binding domain with **11** (Figure 7). The binding mode and key interactions of **11** with TYK2 are highly conserved compared to a co-crystal structure previously reported from a structurally related imidazopyridazine aryl-pyridone series (PDB 6NSL).[37] Additionally, the hinge binding region and pseudo-catalytic Lys642 of TYK2 have similar interactions with **11** as they did with **8**. The pyridonyl-fluoropyridine biaryl system of **11** forms a network of water-mediated H-bond interactions with the TYK2 protein, including Pro694, and Arg738 appears to form a pi-stacking interaction with the terminal fluoropyridine of **11**. Notably, the fluorocyclopropane ring of **11** appears to adopt multiple conformations in the binding pocket of TYK2 proximal to Val603, suggesting the opportunity to fill extra space in this region. The opportunity to fill this space offers a rationale for the improved binding potency of slightly larger substituents, such as the cyclobutyl substituents in Table 3.

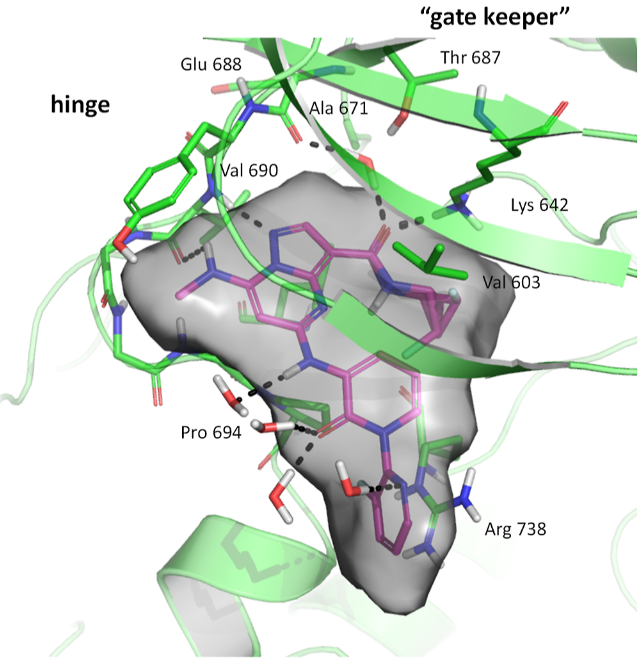

Figure 7. X-ray co-crystal structure of **11** bound to the JH2 domain of TYK2 at 1.71 Å (PDB: 8S99). Dual conformations of the fluorocyclopropyl amide were modeled to account for the observed electron density. The binding mode and key interactions are similar to those previously described for PDB 6NSL.[37]

We next sought to retain the overall potency achieved through the incorporation of a methoxycyclobutyl amide while re-evaluating pyridone substituents (Table 5). The majority of aryl and alkyl groups we evaluated maintained excellent binding potency to the TYK2 JH2 domain (K_D values < 7 pM), with the notable exception of 2-methyl pyridone **33**. As an initial triage strategy, kinetic solubility[42] and human hepatocyte stability were used to narrow our focus to compounds with an opportunity for good absorption and the potential for a lower predicted human dose relative to **11**. The majority of compounds in Table 5 possess reduced human hepatocyte stability relative to **11** and compounds with promising stability (i.e., CL_{pred} < 1.8 mL/min/kg) include **30**, **31**, **34**, **38**, **39**, **45**, and **47**. The remainder of the compounds in Table 5 were not considered for further profiling due to their reduced human hepatocyte stability. With respect to solubility, compounds with saturated (sp^3) substituents on the pyridone ring exhibited a trend for improved solubilities relative to aromatic substituents. One exception is the symmetrical tetrahydropyran **40**, which possessed a kinetic solubility of only 8.2 μM at pH 7.4 (as well as suboptimal hepatocyte CL_{pred}), although the symmetrical oxetane **47** was only slightly improved (15 μM), but with reduced potency in the pSTAT4 IL12 PBMC cellular assay. In general, the aromatic pyridones possessed poor solubilities; the only ones with solubility greater than 10 μM that also exhibited promising hepatocyte stability were compounds **30**, **34**, and **39**. Compounds selected for further profiling exhibited cellular pSTAT4 IL12 PBMC IC_{50}s less than 10 nM, kinetic solubilities greater than 10 μM, and human hepatocyte clearance less than 2 mL/min/kg and included **30**, **34**, and **39**. This small sub-series was evaluated further for their whole blood potencies, off-target cellular potencies, and permeability and efflux, as measured by a Caco-2 assay (Table 6).

All three compounds were highly selective in the PBMC pSTAT5 assays (Table 4), thus demonstrating a high degree of functional selectivity over JAK1, JAK2, and JAK3. Compounds **30** and **34** possess similar human whole blood potencies, but **34** possessed slightly lower permeability and higher efflux than **30**. Additionally, **30** possessed improved stability in human hepatocytes compared to **34**. Consequently, additional profiling of **34** was discontinued in favor of continued profiling of **30**. Although methyl oxazole **39** also exhibited lower permeability and higher efflux in the Caco-2 assay, this compound was profiled further in a rat pharmacokinetic study because it was also highly potent in IL12-induced pSTAT4 PBMCs (1.8 nM) and showed adequate kinetic solubility (67 μM) and human hepatocyte stability below the limits of quantification.

In mouse pharmacokinetic studies, **17** and **30** exhibited relatively low plasma clearance compared to their respective mouse hepatocyte stabilities. In this respect, they were similar to **11** where hepatocyte stability data overpredicted in vivo plasma clearance. In rat pharmacokinetics studies, **17** and **30** each possessed plasma clearance similar or slightly below their hepatocyte predicted clearance, indicating good IVIVE in rats compared to mice. In contrast, **39** exhibited in vivo clearance in rats that was roughly double the hepatocyte in vitro clearance. The improved IVIVE for **17** and **30** in rats compared to **39** suggested continued profiling for each of those compounds. Both **17** and **30** had similar IFNα human whole blood potencies (IC_{50}s = 43 and 51 nM, respectively), but a comparison of their predicted human clearance based on hepatocyte incubations suggested that **30** (human hepatocyte predicted CL = 0.69 mL/min/kg) would have a lower predicted human dose than **17** (human hepatocyte predicted CL = 2.3 mL/min/kg). The evaluation of **30** in preclinical pharmacokinetic studies revealed reasonably good IVIVE across species, suggesting that a human dose prediction using IVIVE from in vitro human hepatocyte data would be warranted. Using the Wajima allometry model[44] as well as PBPK-gut models,[45] the predicted human plasma clearance for **30** was 1.7−7.5 mL/min/kg, the predicted human volume of distribution at steady state was 1.2−10 L/kg and the human bioavailability was predicted to be 44−65%. Coverage of the target trough concentration of 51 nM (human WB IFNα IC_{50}) for 24 h translated to a predicted once-daily oral human dose of 4−42 mg/day. Consequently, **30** (TAK-279, formerly NDI-034858) was chosen for more extensive characterization.

https://doi.org/10.1021/acs.jmedchem.3c00600

Downloaded from https://papernode.pages.dev

Table 5. Pyridone Substituent SAR for a Series of *trans* Methoxy Cyclobutylamide Pyrazolo-Pyrimidine TYK2 JH2 Inhibitors

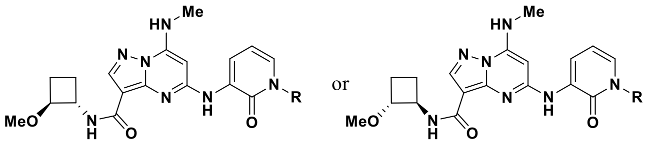

Cpd[a]	R	ALogP[b]	TYK2-JH2 K_D[a,c] (nM)	hPPB Fu[c] (%)	PBMC IL12 / pSTAT4 IC_{50}[c] (nM)	Kin Sol pH 7.4[c] (μM)	Hum Hep CL_{pred}[c] (mL/min/kg)
29	iPr	2.2	0.0040	14	2.8	317	4.8
30[e]	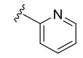	2.0	0.0038^{d}	23	6.7	32^{d}	0.69^{f}
31	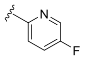	2.1	0.0025^{d}	21	8.1	5.0	1.1
32	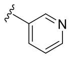	2.0	0.0015^{d}	32	13	2.3	2.6
33	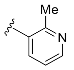	2.3	0.105^{d}	27	--	84	3.3
34	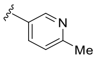	2.3	0.0045^{d}	23	2.2	71	1.7
35	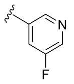	2.1	0.0066^{d}	24	--	2.3	7.7
36	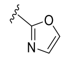	1.6	0.0056^{d}	21	6.4	23	5.9
37	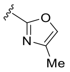	1.9	0.0020^{d}	12	2.0	2.5	2.3
38	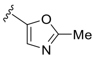	1.9	0.0016^{d}	22	9.8	4.5	0.68
39	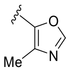	1.9	0.0028	34	1.8	67	<LoQ
40	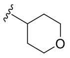	1.9	0.0036^{d}	36	39	8.2	2.1
41	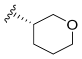	1.9	0.0057^{d}	35	22	283	4.0
42	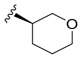	1.9	0.0044d	32	6.8	255	3.1
43	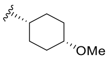	2.7	0.0042^{d}	14	9.6	28	10
44	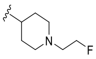	2.2	0.0036	35	16	156	6.2
45	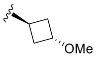	1.9	0.0024^{d}	23	--	149	1.3
46	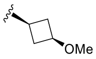	1.9	0.0021^{d}	21	--	52	3.9
47	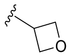	1.2	0.0069^{d}	32	19	15	1.4

[a] Only data for the most potent enantiomer shown, absolute stereochemistry not determined. [b] A log *P* calculated as described in ref 40. [c] Unless otherwise noted, each assay run was performed with $n = 1$. [d] Value is the average of $n \geq 2$ assay runs. [e] Stereochemistry determined to be *R*,*R* by small molecule X-ray crystallography (Figure 8). [f] Hepatopac low turnover assay.

The *R*,*R* stereochemistry on the chiral cyclobutyl ring of **30** was confirmed through single compound X-ray crystallography (Figure 8). The pyridone-pyridine biaryl moiety of this X-ray structure adopts a dihedral angle of 51.4°, which is slightly skewed compared to the nearly orthogonal dihedral angle observed in the TYK2 JH2 bound conformation of **30** (78.7°, vide infra). Evaluation of compound **30** in a panel of CYP450 enzymes indicated a low likelihood of CYP inhibition at physiologically relevant concentrations [CYP450 IC_{50}s > 30 μM for CYP1A2, CYP2C9, and CYP2D6; 19 μM for CYP2C19, 8.3 μM for CYP3A4 (midazolam), and 2.0 μM for CYP3A4 (testosterone)]. Additionally, compound **30** possessed low activation of PXR with only 26% activation relative to the rifampicin control at a concentration of 30 μM. In a panel of 87 enzymes, ion channels, and receptors, a 10 μM concentration of **30** bound to only 2 targets greater than 50% (LCK at 54% and the adenosine transporter at 53%). In a panel of 631 kinases [(ATP) = 10 μM], 1 μM of **30** inhibited only one kinase at greater than 50% (PIP5K1C at 54% inhibition, Figure 9). Moreover, **30** inhibits neither PDE4D (IC_{50} > 10 μM) nor hERG (IC_{50} > 30 μM in the patch clamp assay).

Downloaded from https://papernode.pages.dev

Table 6. In Vitro and In Vivo[a] ADME Properties of Key Compounds

Cpd	Caco-2 P_{app}[b] A−B/ER	Species	Hepatocyte CL_{pred}[b] (mL/min/kg)	PPB Fu[b] (%)	CL_{obs} (mL/min/kg)	$t_{1/2}$(h)	Vd (L/Kg)	F (%)
11	15/1.3	mouse	113	1.0	6.5	2.2	0.58	52
		rat	31	3.1	5.7	2.7	0.52	59
		dog	9	13	18	3.0	2.3	51
		cyno	7	14	12	1.4	1.1	97
17	10/2.2	mouse	186	8.2	21	2.1	0.93	
		rat	25	9.6	20	5.9	2.0	30
		dog	12	22				
		cyno	8.6					
30	15/1.0	mouse	136	8.0	16	2.0	1.3	70
		rat	30	15	26	1.2	1.6	37
		dog	15	23	14	5.3	4.0	47
		cyno	15	23	7.0	3.8	1.9	47
39	3.4/7.6	mouse		23	122	1.7	3.2	
		rat	38		68	1.6	2.9	

[a]Compounds were dosed at 1 mpk IV and 10 mpk PO unless otherwise noted; $n = 3$ animals each for IV and PO dosing. [b]Each assay run was performed with $n = 1$.

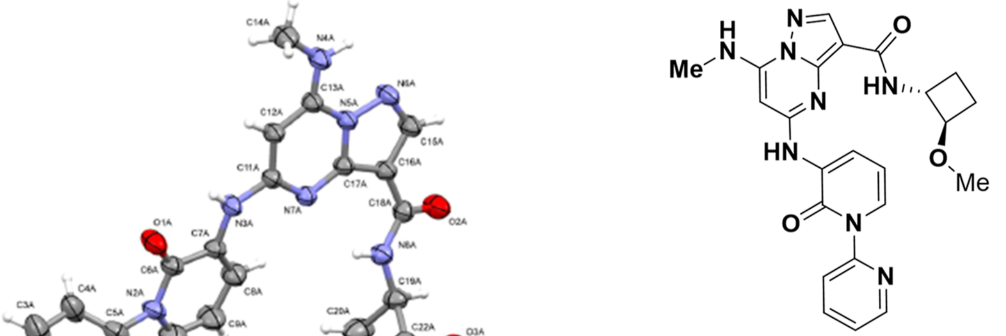

Compound **30**
TAK-279 (formerly NDI-034858)

Figure 8. Single compound X-ray crystallographic representation of **30** (TAK-279, formerly NDI-034858) confirms the (*R*,*R*) absolute stereochemistry in the cyclobutane ring (CSD: 2253269).

We also profiled **30** in a series of binding and cellular assays reflective of JAK1, JAK2, JAK3, and/or TYK2 inhibition. Table 7 summarizes the data sets for compound **30** alongside the data reported for deucravacitinib (**4**).[27,39] Compound **30** was highly selective for binding to the TYK2 JH2 domain (K_D = 0.0038 nM) over the JAK1 and JAK2 JH2 domains (K_Ds = 4975 and 23,000 nM, respectively). In contrast, deucravacitinib (**4**) was reported to bind to the JAK1 JH2 domain with a K_D = 0.33 nM.[39] As expected, based on the low sequence homology between the JH1 and JH2 binding domains for the JAK family kinases, **4** and **30** each exhibit excellent selectivity over binding to the JAK1−3 JH1 domains and the TYK2 JH1 domain.

In cellular and whole blood assays, **30** exhibited potent inhibition of TYK2-dependent signaling pathways. For example, **30** inhibited IFN*α*-stimulated phosphorylation of STAT3 in CD3-positive T-cells as well as IFN*α*-stimulated C−X−C motif chemokine ligand 10 (CXCL10) production in whole blood with IC_{50}s of 1.7 and 22 nM. Additionally, **30** inhibited IL23-stimulated phosphorylation of STAT3 in human CD161 + CD3 + T_H17 cells with an IC_{50} of 3.7 nM. Deucravacitinib (**4**) inhibited these processes in human whole blood and PBMCs with similar potencies.[39] In mouse and rat whole blood, **30** inhibited IFN*α*-stimulated CXCL10 production with somewhat reduced potencies compared to human whole blood (IC_{50}s = 347 and 91 nM, respectively). Compound **30** also inhibited IL12-IL18-stimulated induction of IFN*γ* in whole blood with an IC_{50} = 48 nM.

Compound **30** exhibited a higher level of functional selectivity in cellular and whole blood assays that evaluate signaling through JAK1, JAK2, or JAK3 compared to **4** (Table 7). While neither **4** nor **30** exhibited any activity in assays dependent on JAK2 signaling (pSTAT5 in GM-CSF-stimulated PBMCs, pSTAT5A in EPO-stimulated TF-1 cells), **30** was more selective than **4** in cell assays dependent on JAK1 signaling. For example, in IL2-stimulated $CD3^+$ T-cells, **30** did not inhibit phosphorylation of STAT5 (IC_{50} > 50,000 nM), while compound **4** inhibited this process with an IC_{50} of 592 nM. Similarly, in IL6-stimulated $CD3^+$ T-cells **30** exhibited no inhibition (IC_{50} > 30,000 nM) of phosphorylation of STAT3, while **4** exhibited an IC_{50} of 100 nM. In IL22-stimulated HT-29 cells, **30** also exhibited no inhibition (IC_{50} > 30,000 nM) of phosphorylation of STAT3, compared to **4**, which exhibited an IC_{50} = 158 nM. Together, the data show that the differences in binding selectivity of **4** and **30** to TYK2 compared to JAK1 appear to translate to differences in cellular pharmacology with these compounds, with **30** exhibiting inhibition of TYK2 that is highly selective over pharmacology mediated by JAK1 or JAK2.

Downloaded from https://papernode.pages.dev

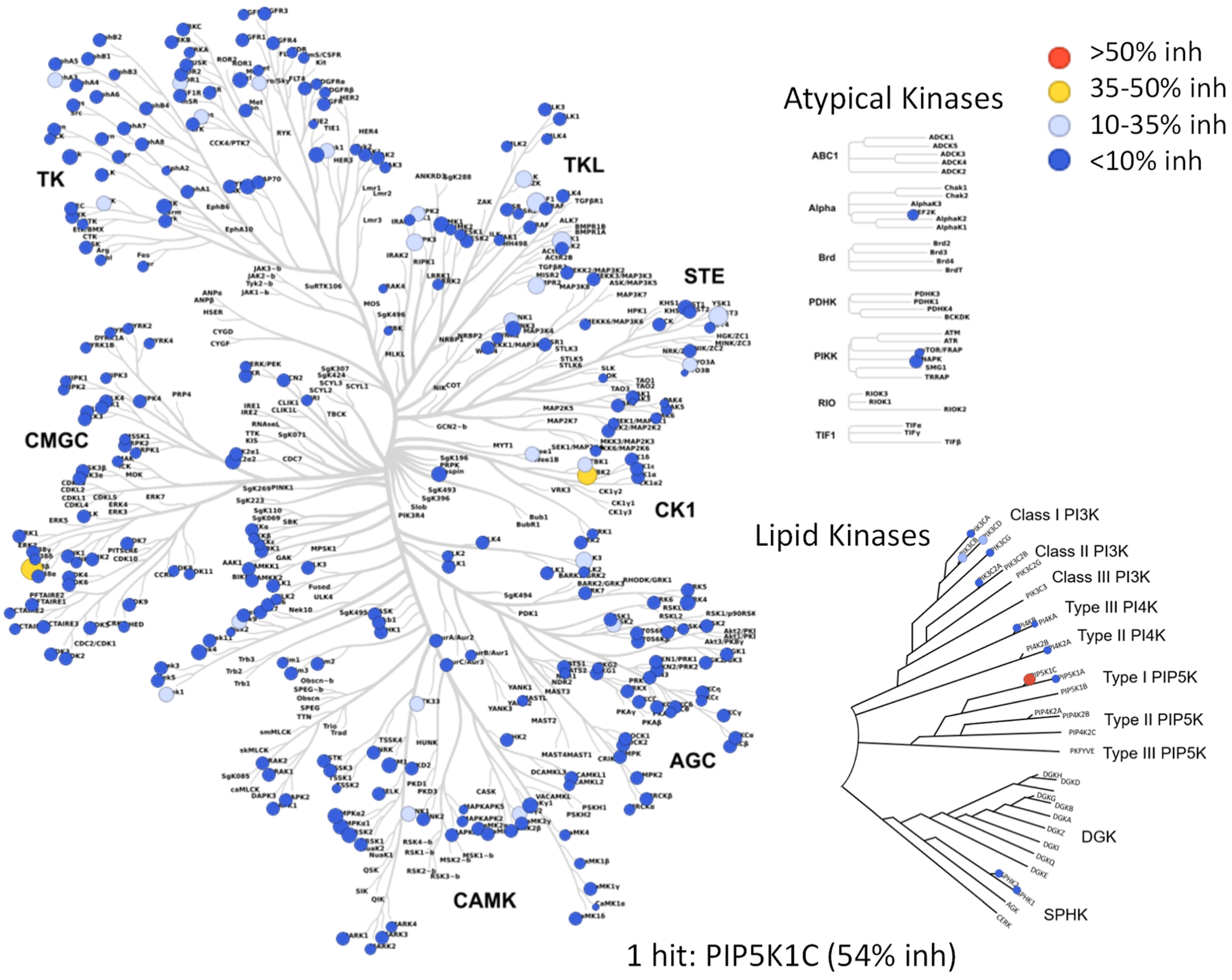

Figure 9. Compound **30** exhibits excellent overall kinome selectivity, with only 1 kinase inhibited at >50% in a panel of 631 kinases ([compound **30**] = 1 μM, [ATP] = 10 μM).

The high selectivity for binding of **30** to the TYK2 JH2 domain compared to the JH2 domains of JAK1 and JAK2 can be explained through a comparison of the X-ray co-crystal structure of **30** with the TYK2-JH2 domain and a similar modeled pose of **30** with JAK1 and JAK2 using previously reported X-ray co-crystal coordinates (Figure 10).[46,47] The methoxycyclobutyl ring of **30** is an exquisite steric fit into the binding pocket defined by Val603 and Lys642 of TYK2 (Figure 10a,c). In contrast, the Ile597 residue in the JAK1 JH2 domain provides increased steric occlusion of this binding pocket in JAK1, leading to its weak binding potency to the JAK1 JH2 domain (JAK1 JH2 K_D = 5000 nM for **30**, Figure 10b,d). Similarly, the Ile559 residue of JAK2 occludes the same binding pocket for **30** (JAK2 JH2 K_D = 12,000 nM, not pictured in Figure 10). The 16-fold improved TYK2 JH2 binding affinity of **30** compared to **11** is notable. We rationalize that some of this improved potency may be due to the improved steric fit of the larger cyclobutyl moiety of **30** compared to the cyclopropyl ring of **11**. Perhaps even more relevant, however, is the new H-bond that is apparent between the methoxy oxygen of **30** and the pseudo-catalytic Lys642 residue.

Compound **30** was next profiled in the mouse recombinant murine (rm) rmIL23-induced epidermal hyperplasia model described above.[43] BID dosing of **30** for 3 days reduced inflammation and IL17 levels in the IL23-injected ears (Figure 11). To improve exposures after oral dosing for in vivo profiling studies, we used a spray-dry dispersion (SDD) of **30** that would maintain an amorphous form. A comparison of mouse pharmacokinetics with **30** with and without SDD is illustrated in Figure 12. We were pleased to find that the SDD formulation increases overall exposure levels by **30** in mice as well as rats (data not shown). Consequently, we used the SDD form for PK/PD/efficacy studies, which afforded higher exposures and reduced variability.

In a rat model that evaluated IFNγ induction after treatment with rat IL12 and IL18, the SDD form of **30** demonstrated dose-dependent suppression of IFNγ (Figure 13).[48,49] Plasma drug levels at the 5 h timepoint suggests that significant suppression of IFNγ occurs slightly above the rat whole blood IFNα CXCL10 IC_{50} concentration. The most robust suppression of IL12-induced IFNγ occurred at the 30 mg/kg dose, which corresponds to a plasma drug level that was above the IFNα CXCL10 IC_{90} concentration.

We next evaluated **30** in a rat adjuvant-induced arthritis (AIA) model (Figure 14).[50] In this study, doses of 3, 10, and 30 mg/kg BID were assessed, and a dose-dependent reduction in ankle

Downloaded from https://papernode.pages.dev

Table 7. Binding, Cellular, and Whole Blood Potencies for Compound 30 (TAK-279, Formerly NDI-034858) Compared to Literature-Reported Data for Deucravacitinib (4)

Assay	Cells (pathway)	TAK-279 (**30**)[a]	Deucravacitinib (**4**)
human TYK2 JH2 (K_D or K_i, nM)	(TYK2)	0.0038 (K_D)	0.02 (K_i)[39]
mouse TYK2 JH2 K_D (nM)	(TYK2)	0.067	
human JAK1 JH2 K_D (nM)	(JAK1)	4975	0.33[39]
human JAK2 JH2 K_D (nM)	(JAK2)	23,000	
human JAKs 1−3 and TYK2 JH1 K_D (nM)		>30,000	>10,000[27]
human IFNα pSTAT3 (CD3+) IC_{50} (nM)	PBMC (TYK2)	1.7	3[39]
human IFNα CXCL10 IC_{50} (nM)	WB (TYK2)	22	6[37]
mouse IFNα CXCL10 IC_{50} (nM)	WB (TYK2)	347	
rat IFNα CXCL10 IC_{50} (nM)	WB (TYK2)	91[b]	
IL23 pSTAT3 (CD3 + CD161 + Th17) IC_{50} (nM)	PBMC (TYK2)	3.7	9[27]
IL12-IL18 IFNγ IC_{50} (nM)	WB (TYK2)	48	
GM-CSF pSTAT5 IC_{50} (nM)	PBMC (JAK2)	>50,000	
EPO pSTAT5A IC_{50} (nM)	TF-1 (JAK2)		>10,000[39]
IL2 pSTAT5 IC_{50} (nM)	PBMC (JAKs 1/3)	>50,000	592[27]
IL4 pSTAT6 (CD3+) IC_{50} (nM)	PBMC (JAKs 1/3)	>30,000	
IL6 pSTAT3 (CD3+) IC_{50} (nM)	PBMC (JAKs 1/2)	>30,000	100[39]
IL13 pSTAT6 IC_{50} (nM)	PBMC (JAK 1)	>30,000	2091[27]
IL22 pSTAT3 IC_{50} (nM)	HT-29 (JAKs 1/2)	>30,000	158[39]
IFNγ SEAP IC_{50} (nM)	HEK-dual (JAKs 1/2)	>27,000	

[a] Unless otherwise noted, the value is the average (geometric mean) of $n \geq 2$ assay runs. [b] Data reported for $n = 1$.

diameter was observed at all 3 dose levels. The lowest dose of 3 mg/kg exhibited a modest but significant reduction of ankle diameter relative to vehicle-treated rats. At this dose, the drug concentration at the trough dropped slightly below the rat whole blood IFNα CXCL10 IC_{50}. The most robust efficacy was observed at the 30 mg/kg BID dose, which was comparable to the efficacy observed with dexamethasone. The rat plasma trough drug levels at this dose exceeded the rat whole blood IFNα CXCL10 IC_{90}, demonstrating that robust efficacy requires sustained high levels of TYK2 inhibition and that maximal efficacy can be achieved with >90% inhibition of TYK2 in this model.

Next, **30** was evaluated in a seven-day mouse anti-CD40 colitis model[51] at doses of 15 and 90 mg/kg BID (Figure 15). Both doses exhibited significant (relative to vehicle-treated mice) and dose-dependent reductions in colon weight/length ratios and reductions in a summed colon histology score, which included measures of inflammation, gland loss, erosion, and hyperplasia. Positive controls included anti-IL-12 and anti-TNFα monoclonal antibodies (mAbs), and both positive controls exhibited reduction, in summed histology scores. The anti-IL12 mAb, but not the anti-TNFα mAb, exhibited a reduction in colon weight/length ratio. In a pilot mouse PK study prior to the anti-CD40 colitis study, the 15 mg/kg BID dose covered only the mouse WB IFNα CXCL10 IC_{50} at trough, while the 90 mg/kg BID dose covered the IC_{90} at trough. Mouse PK taken at day 7 of this study, however, revealed that the drug concentrations at both doses covered the IC_{90} at the 2- and 8 h timepoints, albeit with the 90 mg/kg BID dose achieving higher plasma concentrations than the 15 mg/kg BID dose. Nevertheless, the colon weight/length ratio as well as the summed colon histology scores both exhibited a dose-dependence in efficacy. This study corroborates the AIA data, showing that the increased levels of TYK2 inhibition translate into improved efficacy.

The excellent potency, off-target selectivity, ADME properties, and in vivo efficacy of **30** (TAK-279, formerly NDI-034858) supported its advancement into preclinical toxicology studies. The nonclinical safety profile of **30** was well characterized in a battery of in vitro and in vivo genetic toxicology, safety pharmacology, developmental/reproductive toxicology, and repeat-dose oral toxicology studies. Based on the rat and cynomolgus monkey chronic toxicology studies, adequate safety margins supported further clinical development of **30**. Compound **30** is currently in phase 2 clinical trials for multiple autoimmune and immunological disorders at once-daily oral doses that achieve high coverage at trough concentrations of the human whole blood IFNα CXCL10 (i.e., >IC_{80}).

Chemistry. The synthesis of a sub-series of pyrazolopyrimidine TYK2 inhibitors is described in Scheme 1. Aminopyrazole **48** was first condensed with diethylmalonate to afford a dihydroxypyrazolopyrimidine core **49**, which was then treated with $POCl_3$ to afford the dichloride **50**.[52] Next, the more reactive chloride adjacent to the pyrazole is displaced with methylamine to yield **51**, which was then protected as a corresponding *tert*-butoxycarbamate **52**. The chloride moiety of **52** was next replaced by amines either under basis conditions with either a nucleophilic amine or through Buchwald coupling conditions to give **53**. Compound **53** could be converted to final TYK2 inhibitors in two different ways. First, the ester was hydrolyzed to form acid **54**, which in turn is converted to amides **55** via standard amide-bond-forming coupling conditions. Deprotection of the Boc group then afforded the final inhibitors. Alternatively, the Boc group of **53** was deprotected and the ester hydrolyzed to afford **56**, which then underwent amide bond formation to afford the final compounds. For compounds in which the R and/or R′ groups are chiral, enantiomers were typically resolved through chiral chromatography at multiple stages through intermediates **53**−**56**.

A slightly different series of steps was used to synthesize pyridones **10**, **11**, **13**−**16**, **19**−**24**, and **26**−**28** (Scheme 2). Synthetic intermediate **52** was first hydrolyzed to afford acid **57**, which then underwent amide bond formation to afford amides **58**. These amides were then coupled with aminopyridone **59** to yield the common intermediate **60**. Racemates of **60** could be resolved into the respective pure enantiomers either using chiral chromatography on **60**, or they were deprotected first before chiral separation to afford the pure deprotected enantiomers **10**, **11**, **13**−**16**, **19**−**24**, and **26**−**28**.

The synthesis of methoxycyclobutane amides **17**, **18**, and **29**−**47** is illustrated in Scheme 3. Amide **58** was generated from a standard amide bond coupling through the reaction of acid **57** with the corresponding *trans* aminocyclobutanol, which then underwent amide bond formation to afford **58**. After formation

Downloaded from https://papernode.pages.dev

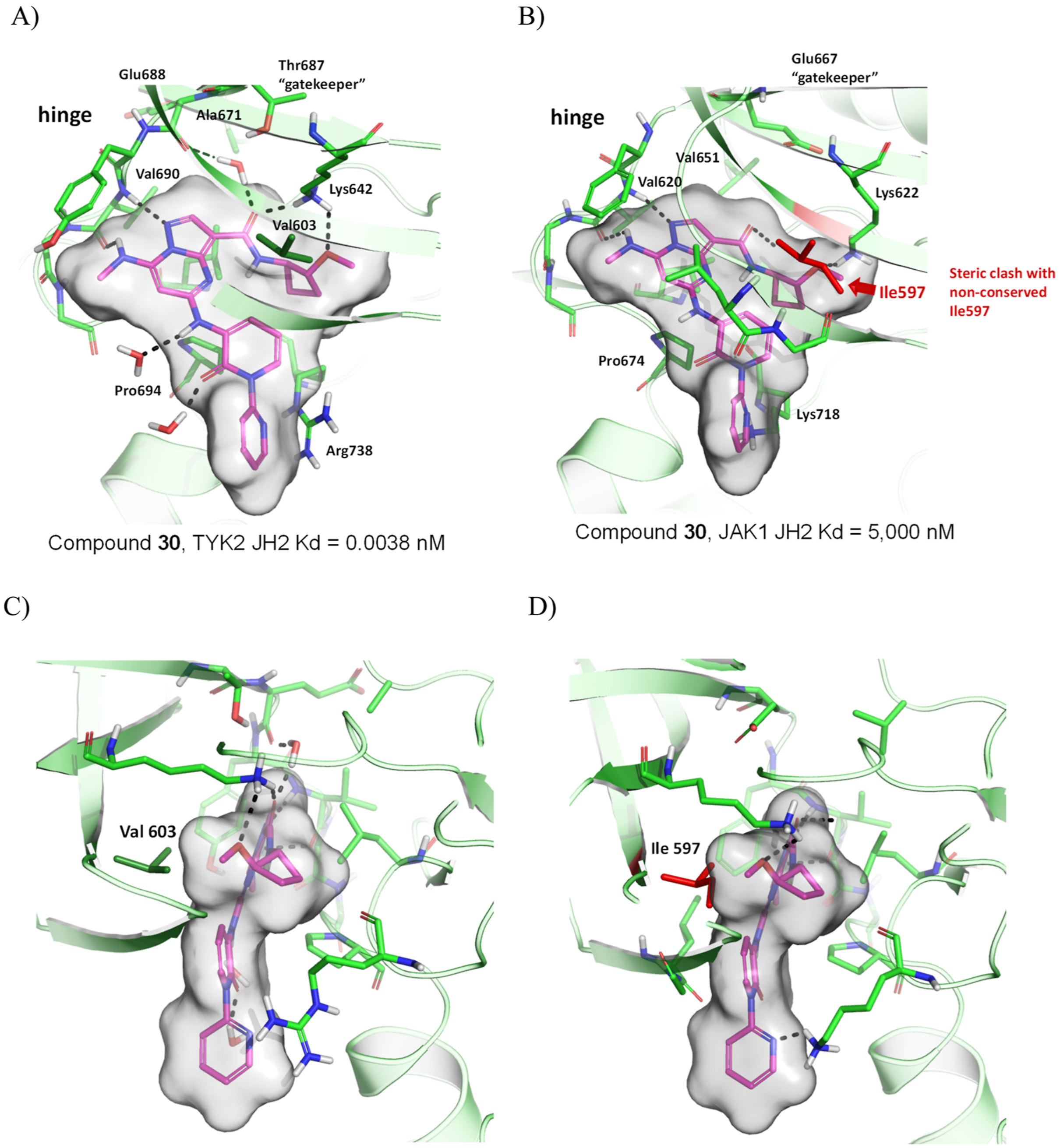

Figure 10. Structural rationale for the high selectivity of the inhibition of TYK2 over inhibition of JAK1 and JAK2 for **30**. (A) Compound **30** bound to the JH2 domain of TYK2 (1.83 Å, PDB 8S9A). (B) Compound **30** docked into the binding pocket of the JAK1 JH2 domain (modeled from PDB 4L00).[46] Note that a similar unproductive steric interaction is present in the JAK2 binding pocket with Ile559 and the cyclobutoxy substituent of **30** (see PDB 5UT6).[47] (C) Close-up view of the methoxycyclobutyl amide of **30** bound to the JH2 domain of TYK2. (D) Modeled view of the methoxycyclobutyl amide of **30** bound to the JAK1 JH2 domain.

of the methyl ether **61**, which was performed under the aegis of tetramethylammonium tetrafluoroborate, Buchwald coupling of a series of pyridone amines **62** afforded intermediate **63**. Racemates of **63** were resolved into the respective pure enantiomers either using chiral chromatography on **63** or they were deprotected first before chiral separation to afford the pure deprotected enantiomers **17**, **18**, and **29**−**47**.

■ CONCLUSIONS

In conclusion, we describe the optimization of a series of potent and highly selective TYK2 JH2 inhibitors through the use of multiple orthogonal structural and computational methods, including virtual screening, FEP+ potency and solubility predictions, a computational RRCK predictive permeability model, and SBDD. A strategy to pursue pseudokinase domain (JH2) TYK2 inhibitors was crucial for achieving high selectivity over JAK1, JAK2, and JAK3 JH1 domains.[19,53,54] We used docking and SBDD to improve selectivity of the initial pyrazolopyrimidine series over PDE4D, and we were guided by FEP potency predictions and SBDD to identify a methoxycyclobutyl amide moiety that enhances binding to the hTYK2 JH2 domain to achieve a K_D < 5 pM. Importantly, **30** is highly selective over the broader kinome, as well as against the JAK1 and JAK2 JH2 pseudokinase domains, with binding

Downloaded from https://papernode.pages.dev

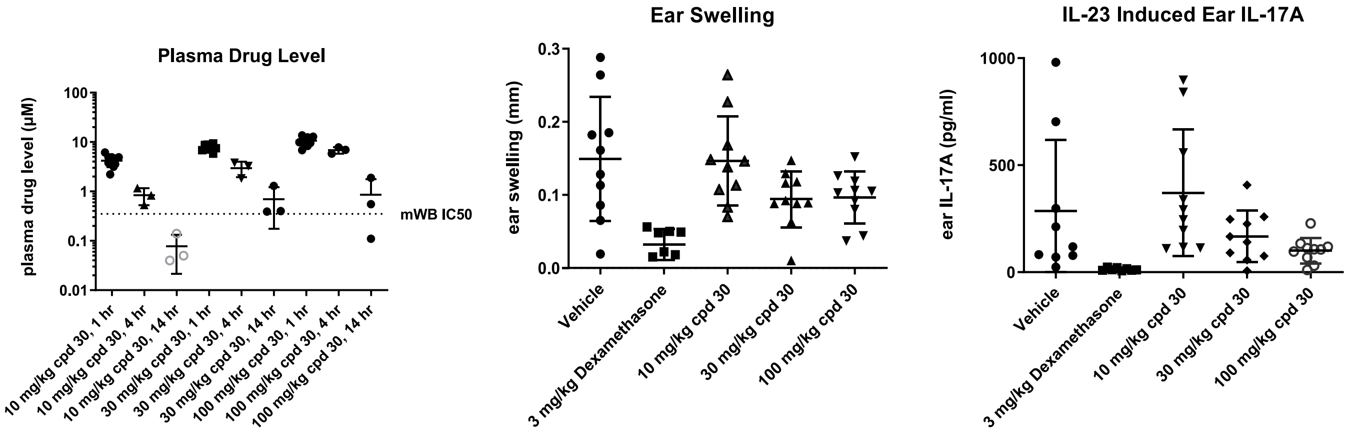

Figure 11. Mouse IL23 model with **30** (n = 3 for the PK group and n = 10 for the efficacy group).

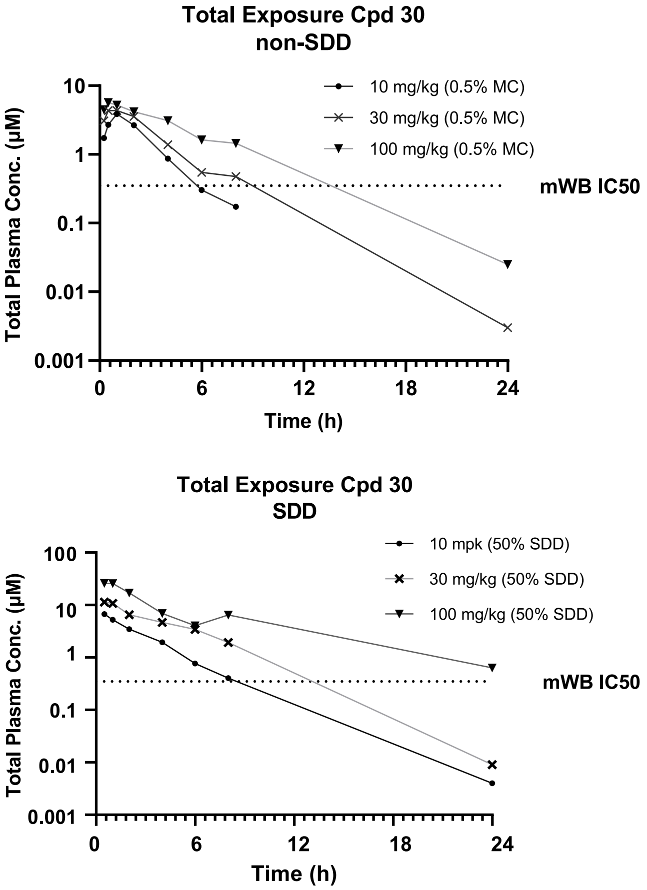

Figure 12. Spray-dried dispersion (SDD) vs non-SDD mouse PK of **30** (n = 3/group) in comparison to the mouse WB IFNα CXCL10 IC_{50}.

A)

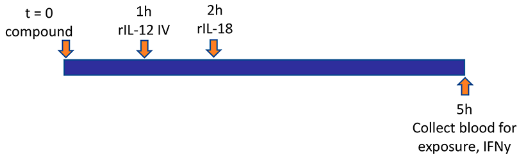

Cmpd 30 Dose	C_{plasma} 5 h (nM)	C_{plasma}/ rWB IC_{50}	% suppression vs vehicle	p value
1 mg/kg	49 (± 8)	0.5	16	-
3 mg/kg	124 (± 12)	1.4	77	0.001
10 mg/kg	584 (± 110)	6.4	87	0.001
30 mg/kg	1483 (± 352)	16	100	0.001

rWB IC_{50} (IFNα mediated IP-10): 91 nM

B)

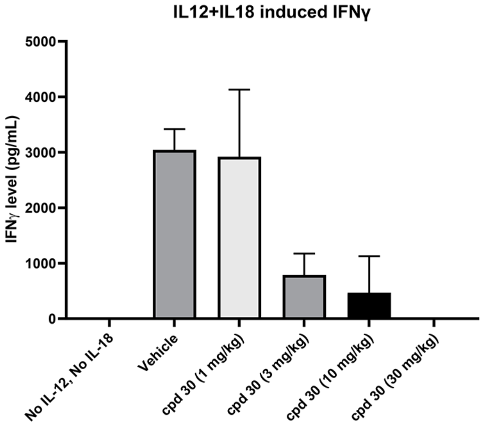

Figure 13. Rat in vivo PD model of the inhibition of IL12/IL18-induced IFNγ production by **30** (SDD formulation). (A) Study design schematic illustrating administration of **30** (n = 5/group) followed by administration of IL12 (IV, 1 h) and IL18 (IV, 2 h) before collecting blood and IFNγ readouts at 5 h. The 5 h plasma concentrations of **30** after administration of 1, 3, 10, and 30 mg/kg doses is also illustrated. At doses of 3−30 mg/kg, the concentration of **30** exceeded the rat whole blood IFNα CXCL10 IC_{50}, with the 30 mg/kg dose exceeding the rat whole blood IFNα CXCL10 IC_{90}. (B) Dose-dependent reduction in IFNγ relative to vehicle-treated rats was noted with treatment of 1−30 mg/kg. While the 1 mg/kg dose was similar to vehicle-treated rats, the 3 and 10 mg/kg doses exhibited 77 and 87% IFNγ suppression relative to vehicle and the 30 mg/kg dose suppressed IFNγ by 100%.

selectivity over a million-fold over these JH2 domains. The structural basis for the high selectivity of compound **30** over the JH2 domains of JAK1 and JAK2 is described, and the accompanying cellular data suggests that even at high levels of inhibition of TYK2 in vivo, very low inhibition of JAK1 or JAK2 is expected with compound **30**.

Furthermore, we show that a sustained high level of TYK2 inhibition in vivo (benchmarked by a WB IFNα CXCL10 assay) confers improved efficacy in a rat AIA model and a mouse anti-CD40-induced colitis model, compared to only 50% inhibition at trough. The ability to achieve high levels of TYK2 inhibition without the accompanying safety risks of JAK1, JAK2, or JAK3

Downloaded from https://papernode.pages.dev

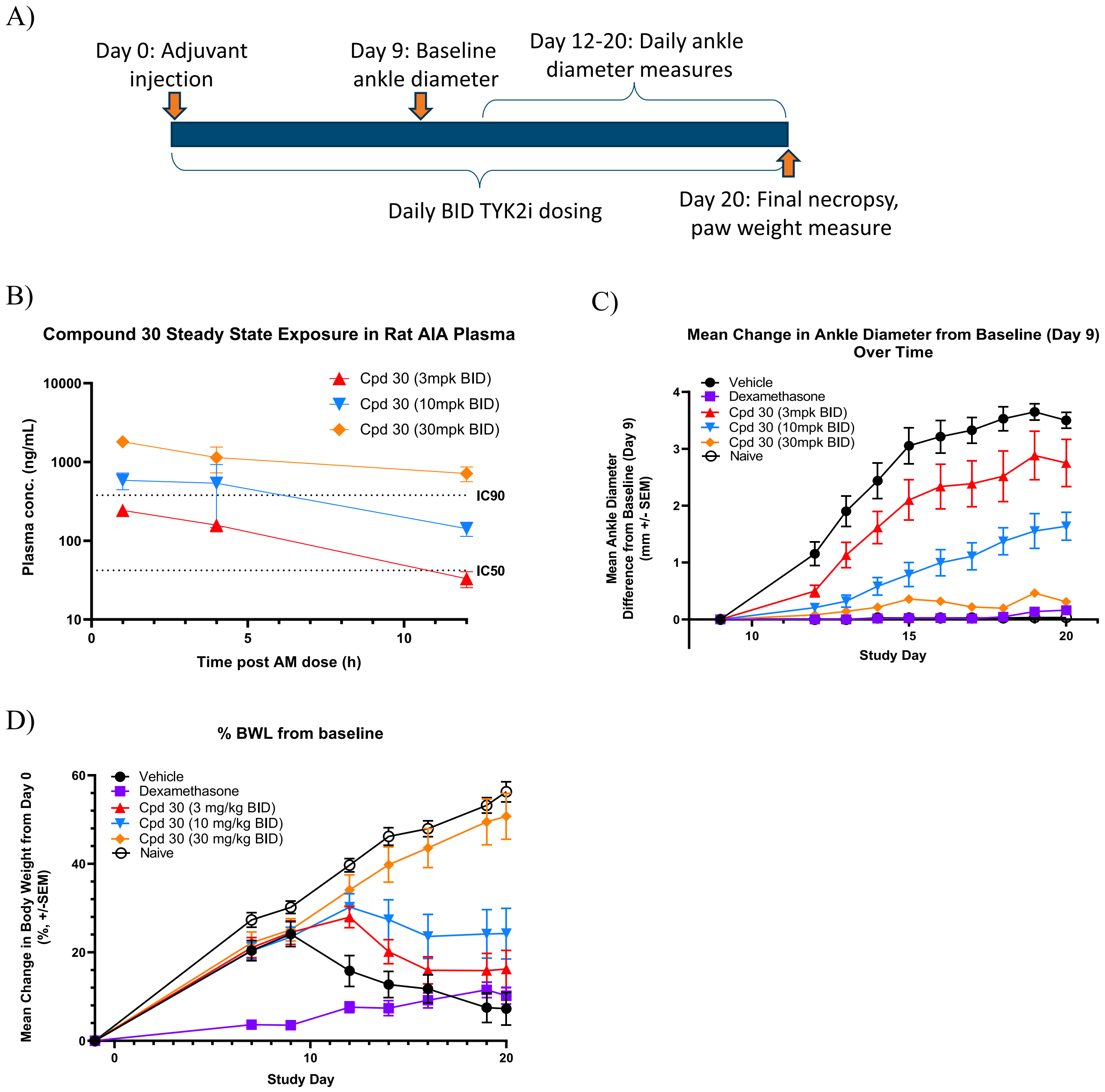

Figure 14. Rat AIA model with **30** ($n = 9$/group). (A) Schematic illustrating the study design in rats. (B) Rat plasma drug levels at day 19 of dosing **30**. Trough levels of the rat WB IFNα CXCL10 IC_{50} were covered for ∼22 h per day at the 3 mg/kg BID dose, while the rat WB IFNα CXCL10 IC_{90} was covered for 24 h a day at the 30 mg/kg BID dose. (C) Statistically significant and dose-dependent reduction in ankle diameter was observed at doses of 3, 10, and 30 mg/kg in the rat AIA model with **30**. (D) Rats dosed with dexamethasone exhibited a reduction in body weight, while rats dosed with **30** exhibited an increase in body weight similar to naïve rats.

inhibition was a key goal we set out to achieve and afforded compound **30** as a potential best-in-class TYK2 inhibitor.

■ EXPERIMENTAL SECTION

All reagents and solvents used were purchased from commercial sources and used without further purification. All reactions were performed under an atmosphere of dry nitrogen, unless otherwise noted. All solvents and reagents were purchased from commercial sources and used as received. ^1H NMR spectra were obtained using a Bruker 300, 400, or 500 MHz spectrometer at 27 °C; chemical shifts are expressed in parts per million (ppm, δ units) and are referenced to the residual mono-^1H isomer of the solvent ($CHCl_3$: 7.24 ppm; $CHDCl_2$: 5.32 ppm; $CD_3S(=O)CD_2H$: 2.49 ppm). Coupling constants are given in units of hertz (Hz). Splitting patterns describe apparent multiplicities and are designated as s (singlet), d (doublet), t (triplet), q (quartet), m (multiplet), and br s (broad singlet). ^{13}C NMR was obtained using a Bruker 125 MHz spectrometer at 27 °C; chemical shifts are expressed in ppm (δ) and are referenced to the perdeuterated NMR solvent ($CHCl_3$: 77.0 ppm; $CHDCl_2$: 54.0 ppm; CD_3SOCD_2H: 39.50 ppm). ^{19}F NMR was obtained using a Bruker 282 or 470 MHz spectrometer at 27 °C unless otherwise noted; chemical shifts are expressed in ppm (δ). ^{19}F chemical shifts were automatically referenced in Topspin (Bruker Instruments) according to the resonance frequency of the perdeuterated lock solvent using the IUPAC ratios. LC−MS was carried out using a Waters UPLC fitted with a Waters SQD mass spectrometer (column temperature = 30 °C, UV = 210−400 nm; electrospray ionization with positive/negative switching) at a flow rate of 1 mL/min using a solvent system of 98% A + 2% B to 2% A + 98% B over 1.5 min, where A = 0.1% formic acid in water (for acidic work) or 0.1%

Downloaded from https://papernode.pages.dev

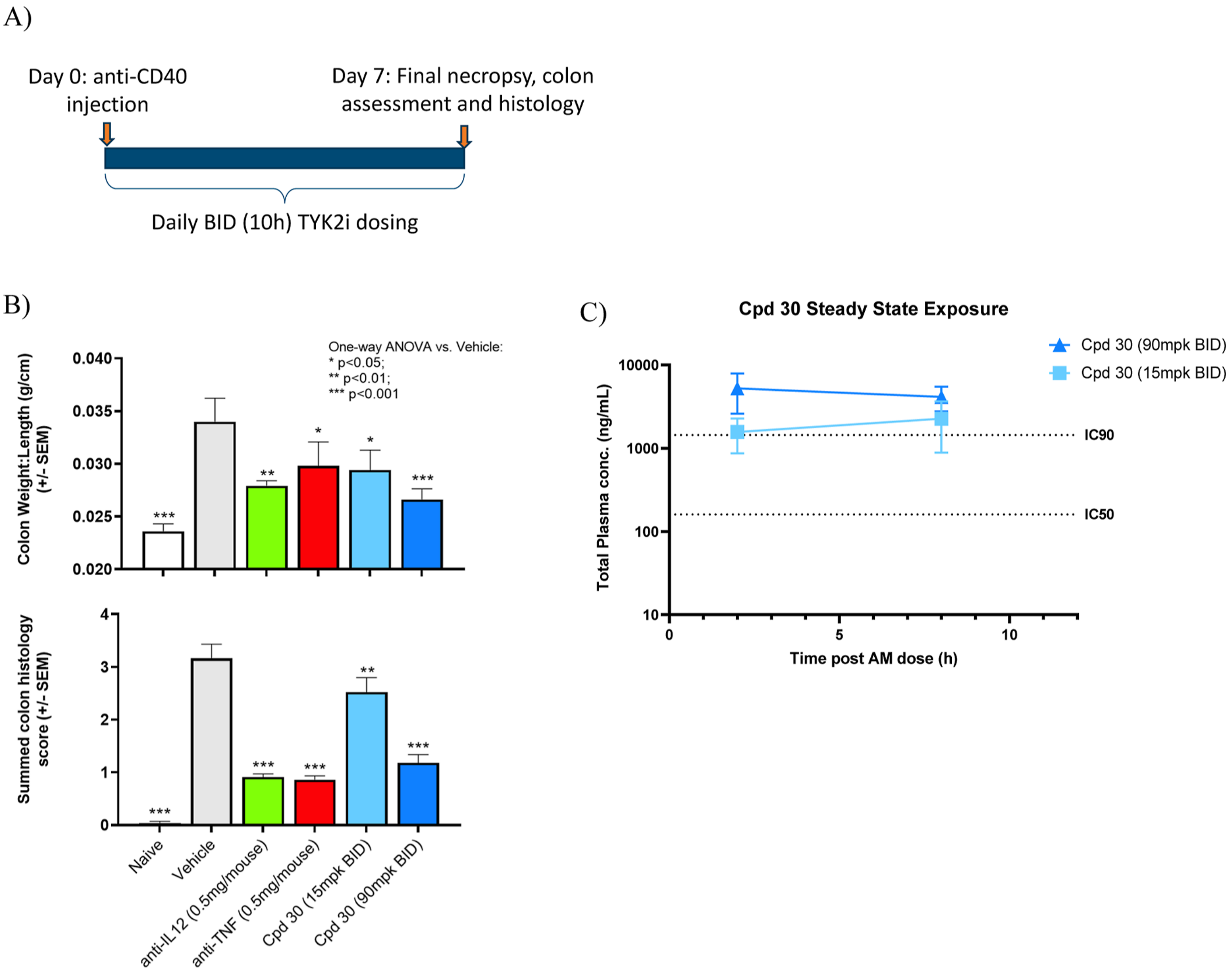

Figure 15. Mouse anti-CD40 colitis model with **30** at doses of 15 and 90 mg/kg BID. (A) Schematic illustrating the study design in mice ($n = 10$/group). (B) Statistically significant and dose-dependent colon weight/length ratio was observed at doses of 15 and 90 mg/kg in the mouse colitis model with **30** compared to vehicle-control-treated mice. Additionally, mice dosed with **30** demonstrated statistically significant and dose-dependent reduction in summed colon histology scores, including measures of inflammation, gland loss, erosion, and hyperplasia. Positive controls included anti-IL12 and an anti-TNFα monoclonal antibody. (C) Mouse plasma drug exposure levels at day 7 of dosing **30** ($n = 5$/timepoint). Drug levels at 8 h post dose exceeded the mouse WB IFNα CXCL10 IC$_{90}$ at both the 15 and 90 mg/kg BID doses.

ammonium hydroxide in water (for basic work) and B = 0.1% formic acid in acetonitrile (for acidic work) or acetonitrile (for basic work). For acidic analysis, the column used was a Waters Acquity HSS T3 (1.8 μm, 2.1 × 30 mm), for basic analysis, the column used was a Waters Acquity BEH C18 (1.7 μm, 2.1 × 30 mm). Reported molecular ions correspond to $[M + H]^+$ unless otherwise noted; for molecules with multiple isotopic patterns (Br, Cl, etc.), the reported value is the one obtained for the lowest isotope mass unless otherwise specified. Thin layer chromatography was performed using EMD silica gel 60 F$_{254}$ plates, which were visualized using either UV light, reversibly stained with iodine (I_2 absorbed on silica), or a stain prepared by dissolving 2 g of $KMnO_4$ and 12 g of Na_2CO_3 in 200 mL of H_2O. Column chromatography was performed using RediSep R$_f$ preloaded silica gel cartridges on Teledyne ISCO CombiFlash Companion automated purification systems. All final compounds are >95% pure by HPLC analysis.

Synthesis of Compound 7, as Described in Scheme 1. *Ethyl 5,7-Dihydroxypyrazolo[1,5-a]pyrimidine-3-carboxylate (**49**).* To a solution of **48** (10 g, 64.45 mmol, 1.0 equiv) in ethanol (300 mL) was added diethyl malonate (20.65 g, 128.9 mmol, 2.0 equiv) followed by dropwise the addition of sodium ethoxide (74.97 g, 21% ethanol solution, 3.59 equiv). The reaction mixture was stirred with heating under reflux for 18 h. After completion of the reaction, the mixture was concentrated under reduced pressure to obtain a residue, which was dissolved in water and acidified with concentrated hydrochloric acid to pH ∼ 3−4. The precipitated solid was filtered, washed with water and diethyl ether, and dried to obtain pure **49** (10 g, 70%). MS(ES): m/z 224.2 $[M + H]^+$.

*Ethyl 5,7-Dichloropyrazolo[1,5-a]pyrimidine-3-carboxylate (**50**).* To a mixture of **49** (3 g, 13.44 mmol, 1.0 equiv) in phosphorous oxychloride (8.7 mL), was added diethyl aniline (3.37 g, 22.56 mmol, 1.68 equiv). The reaction mixture was stirred at 80 °C for 3 h. After completion of the reaction, the mixture was diluted with ice-cold water, neutralized with a saturated sodium bicarbonate solution, and extracted with dichloromethane. The organic layers were combined, washed with a brine solution, dried over sodium sulfate, and concentrated under reduced pressure to obtain the crude material. This was further purified by column chromatography, and the compound was eluted in 15% ethyl acetate in hexane to obtain pure **50** (3.0 g, 86%). MS(ES): m/z 261 $[M + H]^+$.

*Ethyl 5-Chloro-7-(methylamino)pyrazolo[1,5-a]pyrimidine-3-carboxylate (**51**).* To a solution of **50** (3.0 g, 11.54 mmol, 1.0 equiv) in isopropyl alcohol (30 mL) was added diisopropylethylamine (4.2 mL, 23 mmol, 2.0 equiv) at 0 °C followed by methylamine (6.9 mL, 13

Downloaded from https://papernode.pages.dev

Scheme 1. Synthesis of Compounds 7−9, 12, and 25[a]

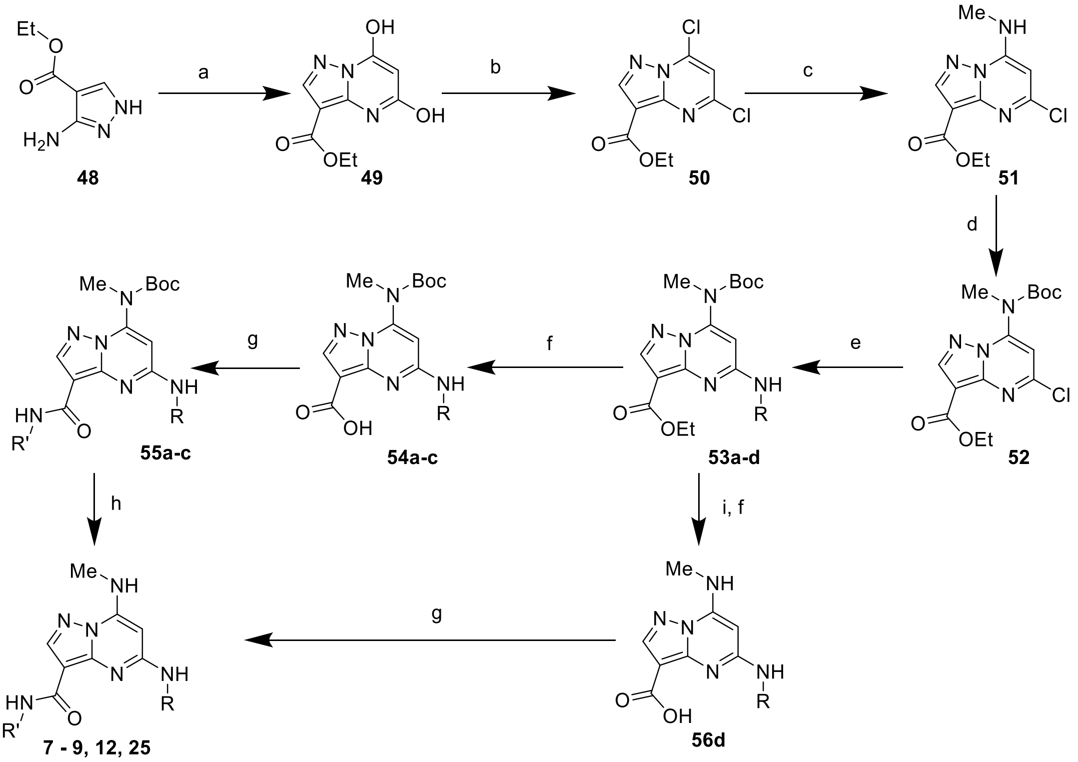

[a]Reagents and conditions: (a) diethylmalonate, NaOEt, EtOH, Δ (70%); (b) $POCl_3$, $PhNEt_2$, 80 °C, 3 h (86%). (c) $MeNH_2$, IPA, DIPEA, 80 °C (95%); (d) Boc_2O, DMAP, dioxane, rt (72%); (e) $R^{a-c}NH_2$, *t*-BuOH, THF, rt or RNH_2, $Pd_2(dba)_3$, Xantphos, Na_2CO_3 or Cs_2CO_3, dioxane, Δ; (f) MeOH, THF, LiOH, H_2O, rt; (g) $R'NH_2$, DMF, HATU, DIPEA, rt; (h) TFA, DCM, 0 °C to rt; (i) dilute HCl. [a−d]Intermediate of compounds **7**−**9**, **12**, and **25**.

Scheme 2. Synthesis of Compounds 10[b], 11[a], 13[c]−16[f], 19[g]−24[l], and 26[m]−28[o][a]

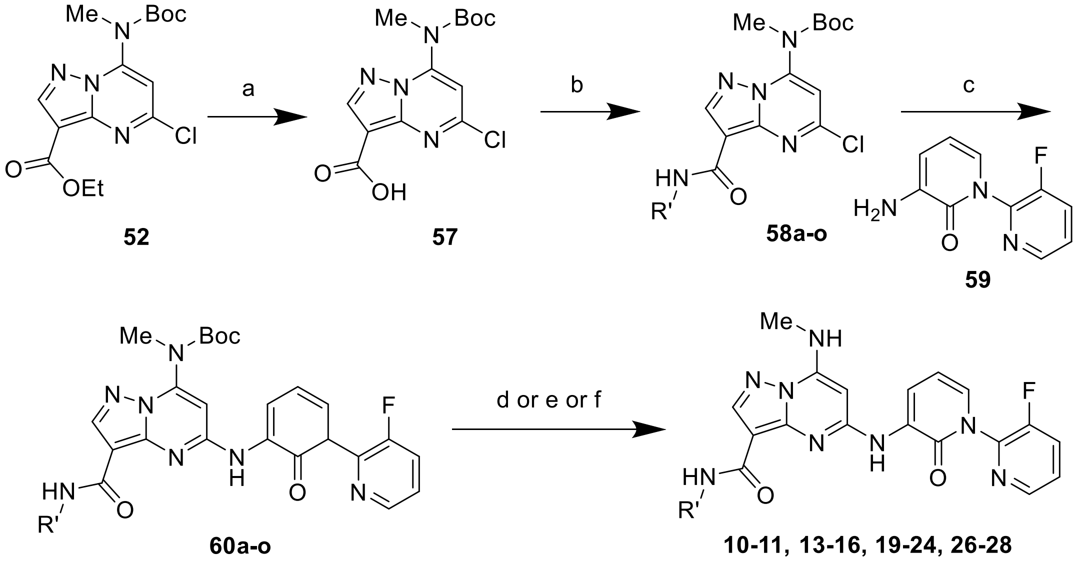

[a]Reagents and conditions: (a) TBTO, tol, Δ (72%); (b_1) $R'^{a-o}NH_2$, DMF, HATU, DIPEA, 20 min, rt or DCM, T3P, RT, 2 h; (b_2) 1-$R'NH_2$, DMF, HATU, DIPEA, 20 min, rt, 2-$(CH_3)_4O(BF_4)$, DCM, rt; (c) **59**, $Pd_2(dba)_3$, Xantphos, Na_2CO_3 or Cs_2CO_3, dioxane; (d) TFA, DCM, 0 °C to rt; (e) 1. chiral separation, 2. TFA, DCM, 0 °C to rt; (f) 1. TFA, DCM, 0 °C to rt, 2. chiral separation. [a−o]Intermediate of compounds **10**, **11**, **13**−**16**, **19**−**24**, and **26**−**28**.

mmol, 1.2 equiv), and the reaction mixture was stirred at 80 °C for 16 h. After completion of the reaction, the mixture was concentrated under reduced pressure to obtain a crude residue. To this residue was added water, and the mixture was extracted with dichloromethane. The organic layers were combined, washed with a brine solution, dried over sodium sulfate, and concentrated under reduced pressure to obtain the crude material. This was further purified by column chromatography, and the compound was eluted in 40% ethyl acetate in hexane to obtain **51**. (2.9 g, 95%). MS(ES): *m*/*z* 310$[M + H]^+$.

https://doi.org/10.1021/acs.jmedchem.3c00600
J. Med. Chem. 2023, 66, 10473−10496

Downloaded from https://papernode.pages.dev

Scheme 3. Synthesis of Compounds 17[a]–18[c], 29[d], 30[a], and 31[e]–47[u][a]

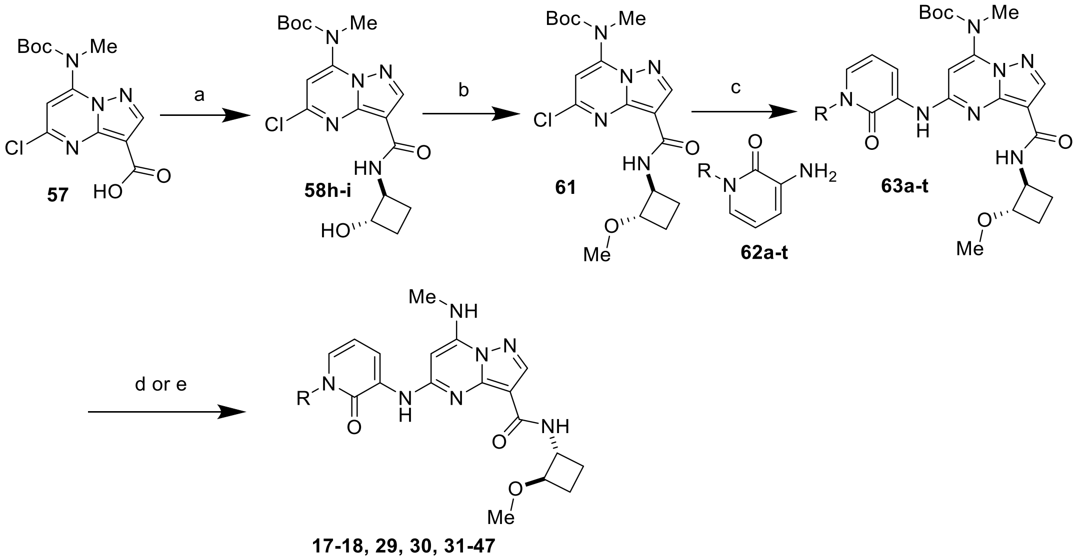

[a]Reagents and conditions: (a) (*trans*)-2-aminocyclobutan-1-ol, DMF, HATU, DIPEA, 20 min, rt; (b) 2,6-di-*tert* butyl-4-Me-pyridine, $(CH_3)_4(BF_4)$, DCM, rt; (c) R-pyridone-NH_2 (**61**), $Pd_2(dba)_3$, Xantphos, Na_2CO_3 or Cs_2CO_3, dioxane; (d) 1. chiral separation, 2. TFA, DCM, 0 °C to rt; (e) 1. TFA, DCM, 0 °C to rt, 2. chiral separation. [a–u] Intermediate of compounds **17**[a]–**18**[c], **29**[d], **30**[a], and **31**[e]–**47**[u].

*Ethyl 7-((tert-Butoxycarbonyl)(methyl)amino)-5-chloropyrazolo-[1,5-a]pyrimidine-3-carboxylate (**52**).* To a solution of **51** (2.9 g, 11.39 mmol, 1.0 equiv) in 1,4-dioxane (15 mL) was added *N*,*N*-dimethylaminopyridine (0.138 g, 1.139 mmol, 0.1 equiv) followed by di-*tert*-butyl dicarbonate (4.79 g, 22.78 mmol, 2.0 equiv), and the reaction mixture was stirred at room temperature for 16 h. After completion of the reaction, the mixture was diluted with water, and the product was extracted with dichloromethane. The organic layers were combined, dried over sodium sulfate, and concentrated under reduced pressure to obtain the crude material. This was further purified by column chromatography, and the compound was eluted in 10% ethyl acetate in hexane to obtain **52**. (2.9 g, 72%). MS(ES): *m*/*z* 355[M + H]$^+$.

*Ethyl 7-((tert-Butoxycarbonyl)(methyl)amino)-5-((3,5-dimethylphenyl)amino)pyrazolo[1,5-a]pyrimidine-3-carboxylate (**53a**).* A mixture of **52** (1.0 g, 2.82 mmol, 1.0 equiv) and 3,5-dimethylaniline (2 mL) was stirred at 80–85 °C for 1.5 h. After completion of the reaction, the mixture was diluted with water, and the product was extracted with dichloromethane. The organic layers were combined, dried over sodium sulfate, and concentrated under reduced pressure to obtain the crude material. This was further purified by column chromatography, and the compound was eluted in 20% ethyl acetate in hexane to obtain **53a** (1.0 g, 81%). MS(ES): *m*/*z* 440.5 [M + H]$^+$.

*7-((tert-Butoxycarbonyl)(methyl)amino)-5-((3,5-dimethylphenyl)amino)pyrazolo[1,5-a]pyrimidine-3-carboxylic Acid (Compound **54a**).* To a solution of **53a** (1.0 g, 2.28 mmol, 1.0 equiv), in tetrahydrofuran/methanol/water (15 mL, 1:1:1), was added lithium hydroxide (0.957 g, 22.8 mmol, 10 equiv). The reaction was stirred at room temperature for 16 h. After completion of the reaction, the mixture was concentrated under reduced pressure to obtain residue. To this residue was added aqueous 1 N hydrochloric acid to adjust pH ~ 6–6.5 at 10 °C. The product was extracted with dichloromethane. The organic layers were combined, washed with a brine solution, dried over sodium sulfate, and concentrated under reduced pressure to obtain **54a** (0.8 g, 85%). MS(ES): *m*/*z* 412 [M + H]$^+$.

*tert-Butyl (3-(Cyclopropylcarbamoyl)-5-((3,5-dimethylphenyl)-amino)pyrazolo[1,5-a]pyrimidin-7-yl)(methyl)carbamate (Compound **55a**).* To a solution of **54a** (0.110 g, 0.267 mmol, 1.0 equiv) in *N*,*N*-dimethylformamide (2 mL) was added 1-[bis(dimethylamino)-methylene]-1*H*-1,2,3-triazolo[4,5-*b*]pyridinium 3-oxid hexafluorophosphate (0.203 g, 0.535 mmol, 2.0 equiv), and the mixture was stirred at room temperature for 20 min. To this mixture was added diisopropylethylamine (0.14 mL, 0.801 mmol, 3.0 equiv), followed by the addition of cyclopropanamine (0.030 g, 0.535 mmol, 2.0 equiv). The reaction mixture was stirred at room temperature for 1 h. After completion of the reaction, the mixture was diluted with water, and the product was extracted with ethyl acetate. The organic layers were combined, washed with a brine solution, dried over sodium sulfate, and concentrated under reduced pressure to obtain the crude material. This was further purified by column chromatography, and the compound was eluted in 25% ethyl acetate in hexane to obtain **55a** (0.070 g, 58%). MS(ES): *m*/*z* 451.5 [M + H]$^+$.

*N-Cyclopropyl-5-((3,5-dimethylphenyl)amino)-7-(methylamino)-pyrazolo[1,5-a]pyrimidine-3-carboxamide (Compound **7**).* Compound **55a** (0.070 g, 0.155 mmol, 1.0 equiv) was dissolved in dichloromethane (2 mL), and trifluoroacetic acid (0.1 mL) was added to the reaction mixture. The reaction was stirred at room temperature for 2 h. After completion of the reaction, the mixture was poured into water, basified with a saturated bicarbonate solution, and the product was extracted with ethyl acetate. The organic layers were combined, dried over sodium sulfate, and concentrated under reduced pressure to obtain the crude material. This was further purified by trituration with diethyl ether to obtain pure 7 (0.025 g, 46%). MS(ES): *m*/*z* 351.56 [M + H]$^+$, LCMS purity: 96.68%, HPLC purity: 96.09%, ^{1}H NMR (DMSO-d_6, 400 MHz): 9.32 (s, 1H), 8.14 (s, 1H), 7.97–7.96 (d, *J* = 3.2 Hz, 1H), 7.86–7.85 (d, *J* = 5.2 Hz, 1H), 7.14 (s, 2H), 6.73 (s, 1H), 5.50 (s, 1H), 2.91 (s, 3H), 2.77–2.74 (m, 1H), 2.30 (s, 6H), 0.72–0.67 (m, 2H), 0.35 (m, 2H).

Synthesis of Compound 12, as Described in Scheme 1. *Ethyl 7-((tert-Butoxycarbonyl)(methyl)amino)-5-((3′-fluoro-2-oxo-2H-[1,2′-bipyridin]-3-yl)amino)pyrazolo[1,5-a]pyrimidine-3-carboxylate (Compound **53d**).* To a cooled solution of **52** (0.2 g, 0.56 mmol, 1.0 equiv) and 3-amino-3′-fluoro-2*H*-[1,2′-bipyridin]-2-one (0.114 g, 0.67 mmol, 1.2 equiv) in tetrahydrofuran (4 mL) at 0 °C was added potassium *tert*-butoxide (1 M in tetrahydrofuran; 1.12 mL, 1.12 mmol, 2.0 equiv). The reaction was stirred at room temperature for 2 h. After completion of the reaction, the reaction mixture was transferred into water, and the product was extracted with ethyl acetate. The organic layer was combined, dried over sodium sulfate, and concentrated under reduced pressure to obtain crude material. This was further purified by column chromatography, and the compound was eluted in 25% ethyl acetate in hexane to obtain pure **53d** (0.120 g, 42%); MS (ES): *m*/*z* 524.20 [M + H]$^+$).

5-((3′-Fluoro-2-oxo-2H-[1,2′-bipyridin]-3-yl)amino)-7-(methylamino)pyrazolo[1,5-a]pyrimidine-3-carboxylic Acid (Com-

Downloaded from https://papernode.pages.dev

pound 56d). To a solution of **53d** (0.120 g, 0.22 mmol, 1.0 equiv) in methanol/tetrahydrofuran/water (4 mL, 2:1:1) was added lithium hydroxide (0.055 g, 2.3 mmol, 10 equiv). The reaction was stirred at 60 °C for 16 h. After completion of the reaction, the reaction mixture was concentrated under reduced pressure to obtain residue. To this was added water, followed by hydrochloric acid to adjust pH ∼ 1−2, stirred for 1 h at 10 °C and neutralized by saturated sodium bicarbonate. The product was extracted with dichloromethane. The organic layer was combined, washed with brine solution, dried over sodium sulfate, and concentrated under reduced pressure to obtain crude material. This was further purified by column chromatography, and the compound was eluted in 2.1% methanol in dichloromethane to obtain pure **56d** (0.065 g, 73%); MS (ES): *m/z* 396.12 $[M + H]^+$).

5-((3′-Fluoro-2-oxo-2H-[1,2′-bipyridin]-3-yl)amino)-N-((1S,2R)-2-fluorocyclopropyl)-7-(methylamino)pyrazolo[1,5-a]pyrimidine-3-carboxamide (Compound ***12****).* Compound was synthesized using the procedure for compound **7** to obtain **12** (0.032 g, 28%); MS (ES): *m/z* 453.37 $[M + H]^+$; LCMS purity: 95.20%; HPLC purity: 95.01%; Chiral HPLC: 96.00%; ^{1}H NMR (DMSO-d_6, 400 MHz): 9.02 (s, 1H), 8.53−8.52 (d, *J* = 4.8 Hz, 1H), 8.30−8.28 (d, *J* = 8 Hz, 1H), 8.27 (s, 1H), 8.10−8.05 (d, *J* = 9.2 Hz 1H), 7.99−7.98 (d, *J* = 4.8 Hz, 1H), 7.84−7.83 (d, *J* = 4.4 Hz, 1H), 7.76−7.72 (m, 1H), 7.45−7.43 (d, *J* = 6.8 Hz, 1H), 6.45−6.41 (t, *J* = 6.8 Hz, 1H), 6.26 (s, 1H), 4.83−4.81 (m, 1H), 3.18−3.17 (d, *J* = 5.2 Hz, 1H), 3.03−3.01 (m, 1H), 2.91−2.90 (d, *J* = 4.8 Hz, 3H), 1.30−1.21 (m, 1H)).

Synthesis of Compound 11, as Described in Scheme 2. *7-((tert-Butoxycarbonyl)(methyl)amino)-5-chloropyrazolo[1,5-a]-pyrimidine-3-carboxylic Acid (**57**).* To a suspension of **52** (20 g, 56.37 mmol, 1.0 equiv) in toluene (200 mL) was added tributyltin oxide (67.19 g, 112.73 mmol, 2.0 equiv), and the reaction mixture was heated at 120 °C for 12 h. After completion of the reaction, the reaction mixture was concentrated under reduced pressure to obtain residue, which was dissolved in saturated sodium bicarbonate solution and washed with hexane. The aqueous layer was separated, acidified with 1 N hydrochloric acid to pH ∼ 5−6, and extracted with ethyl acetate. The organic layers were combined, dried over sodium sulfate, and concentrated under reduced pressure to obtain a solid, which was triturated with hexane to obtain pure **57** (13.2 g, 72%). ^{1}H NMR (DMSO-d_6, 400 MHz): 12.63 (s, 1H), 8.63 (s, 1H), 7.55 (s, 1H), 3.31 (s, 3H), 1.29 (s, 9H).

tert-Butyl (5-Chloro-3-(((1R,2S)-2-fluorocyclopropyl)carbamoyl)-pyrazolo[1,5-a]pyrimidin-7-yl)(methyl)carbamate (Compound ***58a****).* To a solution of **57** (10 g, 30.61 mmol, 1.0 equiv) in *N,N*-dimethylformamide (300 mL) was added 1-[Bis(dimethylamino)-methylene]-1*H*-1,2,3-triazolo[4,5-*b*]pyridinium 3-oxid hexafluoro-phosphate (15.12 g, 39.79 mmol, 1.3 equiv) and stirred at room temperature for 15 min. To this was added (1*R*,2*S*)-fluorocyclopropyl-amine tosylate (7.5 g, 30.61 mmol, 1.0 equiv), followed by the addition of diisopropylethylamine (16 mL, 91.83 mmol, 3.0 equiv). The reaction mixture was stirred at room temperature for 5 min. After completion of the reaction, the reaction mixture was transferred into water, and the product was extracted with ethyl acetate. The organic layers were combined, washed with brine solution, dried over sodium sulfate, and concentrated under reduced pressure to obtain crude material. This was further purified by column chromatography, and the compound was eluted in 35% ethyl acetate in hexane to obtain **58a** (6.0 g, 51%). MS (ES): *m/z* 384.8 $[M + H]^+$.

tert-Butyl (5-((3′-Fluoro-2-oxo-2H-[1,2′-bipyridin]-3-yl)amino)-3-(((1R,2S)-2-fluorocyclopropyl)carbamoyl)pyrazolo[1,5-a]pyrimidin-7-yl)(methyl)carbamate (Compound ***60a****).* To a solution of **58a** (12 g, 31.27mmol, 1.0 equiv) in 1,4-dioxane (110 mL) was added **59** (6.42 g, 31.27 mmol, 1.2 equiv) and sodium carbonate (7.2 g, 68.75 mmol, 2.0 equiv). The reaction mixture was degassed for 10 min under argon atmosphere; then, tris(dibenzylideneacetone)dipalladium(0) (1.85 g, 2.03 mmol, 0.05 equiv) and 4,5-bis(diphenylphosphino)-9,9-dimethyl-xanthene (2.3 g, 4.065 mmol, 0.1 equiv) were added, and the reaction mixture was again degassed for 5 min. The reaction was stirred at 100 °C for 4 h. After completion of the reaction, the reaction mixture was cooled to room temperature, transferred into water, and the product was extracted with ethyl acetate. The organic layers were combined, washed with brine solution, dried over sodium sulfate, and concentrated under reduced pressure to obtain crude material. This was further purified by combi flash using 3% methanol in dichloromethane as the eluant to obtain pure **60a** (7.4 g, 43%). MS (ES): *m/z* 553.47 $[M + H]^+$.

N-((1R,2S)-2-Fluorocyclopropyl)-5-((3′-methyl-2-oxo-2H-[1,2′-bi-pyridin]-3-yl)amino)-7-(methylamino)pyrazolo[1,5-a]pyrimidine-3-carboxamide (Compound ***11****).* Compound **60a** (7.4 g, 13 mmol, 1.0 equiv) was dissolved in dichloromethane (2 mL), and trifluoroacetic acid (50 mL) was added to the reaction mixture. The reaction was stirred at room temperature for 1 h. After completion of the reaction, the reaction mixture was transferred into saturated bicarbonate solution, and the product was extracted with dichloromethane. The organic layers were combined, dried over sodium sulfate, and concentrated under reduced pressure to obtain crude material. This was further purified by trituration with diethyl ether to obtain pure **11** (5.25 g, 91%). MS (ES): *m/z* 453.40 $[M + H]^+$, LCMS purity: 100%, HPLC purity: 96.64%, Chiral HPLC: 99.34%,^{1}H NMR (DMSO-d_6, 400 MHz): 9.02 (s, 1H), 8.52−8.51 (d, *J* = 4.4 Hz, 1H), 8.30−8.27 (m, 2H), 8.09−8.05 (t, *J* = 8.8 Hz, 1H), 7.99−7.98 (d, *J* = 4.8 Hz, 1H), 7.84−7.83 (d, *J* = 4.4 Hz, 1H), 7.75−7.71 (m, 1H), 7.44−7.43 (d, *J* = 5.6 Hz, 1H), 6.45−6.41 (t, *J* = 7.2 Hz, 1H), 6.25 (s, 1H), 5.01−4.83 (m, 1H), 3.03−3.00 (m, 1H), 2.91−2.90 (d, *J* = 4.8 Hz, 3H), 1.28−1.22 (m, 1H), 0.96−0.87 (m, 1H).

Synthesis of Compound 30 according to Scheme 3. *Synthesis of Enantiomers of* ***58h−i****.* Compound was synthesized using the general procedure of compound **58a** to obtain isomers **58h−i**. (0.600 g, 58%); MS (ES): *m/z* 410.16 $[M + H]^+$).

Synthesis of Enantiomers ***61****.* To a solution of **58h−i** (1.0 g, 2.52 mmol, 1 equiv) in dichloromethane (20 mL), triethyloxonium tetrafluoroborate (0.957 g, 5.04 mmol, 2.0 equiv) and 2,6-di-*tert*-butyl-4-methylpyridine (1.54 g, 7.56 mmol, 3.0 equiv) was added. The reaction mixture was stirred at room temperature for 4 h. After completion of the reaction, the reaction mixture was transferred to ice-cold water, and the product was extracted with ethyl acetate. The organic layers were combined, washed with brine solution, dried over sodium sulfate, and concentrated under reduced pressure to obtain crude material. This was further purified by 5% methanol in dichloromethane to obtain enantiomers **61** (0.600 g, 58%). MS (ES): *m/z* 410.16 $[M + H]^+$.

General Synthesis of R-Amino-Pyridones (62a−t). *Compound* ***62b*** *(R = 2-Pyridine).* To a solution of 3-aminopyridin-2(1*H*)-one (2 g, 18.18 mmol, 1.0 equiv) in **1**, 4-dioxane (40 mL) and 2-bromopyridine (7.2 g, 45.45 mmol, 2.5 equiv) were added. The reaction mixture was degassed for 10 min under an argon atmosphere, followed by the addition of potassium carbonate (7.5 g, 54.54 mmol, 3.0 equiv), *N,N*-dimethylethylenediamine (0.640 g, 7.27 mmol, 0.4 equiv), and copper iodide (0.692 g, 3.636 mmol, 0.2 equiv). The reaction mixture was heated at 110 °C for 12 h. After completion of the reaction, the reaction mixture was transferred to ice-cold water, and the product was extracted with ethyl acetate. The organic layers were combined, washed with brine solution, dried over sodium sulfate, and concentrated under reduced pressure to obtain crude material. This was further purified with 3% methanol in dichloromethane to obtain **62b** (2 g, 59%). MS (ES): *m/z* 188.20 $[M + H]^+$.

Compound ***63b****.* The compound was synthesized as above from compound **60a** to obtain **63b**. (0.125 g, 61%), MS (ES): 561.25 $[M + H]^+$.

Compounds ***30*** *and* ***ent-30****.* Compounds were synthesized using the general procedure of compound **11** to obtain a deprotected racemic mixture of **30** and **ent-30** (0.105 g, 97%), MS (ES): *m/z* 461.40 $[M + H]^+$, LCMS purity: 98.84%, HPLC purity: 93.86%, Chiral HPLC: 47.78%, 51.75%, ^{1}H NMR (DMSO-d_6, 400 MHz): 9.06 (s, 1H), 8.66 (br s, 1H), 8.36−8.34 (d, *J* = 7.2 Hz, 1H), 8.22 (s, 1H), 8.12−8.07 (m, 1H), 8.05−8.04 (d, *J* = 1.6 Hz, 1H), 7.99−7.97 (d, *J* = 5.2 Hz, 1H), 7.88−7.86 (d, *J* = 8 Hz, 1H), 7.64−7.62 (d, *J* = 7.2 Hz, 1H), 7.57−7.54 (m, 1H), 6.47−6.44 (t, *J* = 7.2 Hz, 1H), 6.24 (s, 1H), 4.36−4.29 (m, 1H), 3.77−3.71 (m, 1H), 3.22 (s, 3H), 2.92−2.91 (d, *J* = 4.8 Hz, 3H), 2.18−2.06 (m, 2H), 1.56−1.49 (m, 1H), 1.46−1.39 (m, 1H).

Compound ***30****: N-((1R,2R)-2-methoxycyclobutyl)-7-(methylamino)-5-((2-oxo-2H-[1,2′-bipyridin]-3-yl)amino)pyrazolo[1,5-a]-*

Downloaded from https://papernode.pages.dev

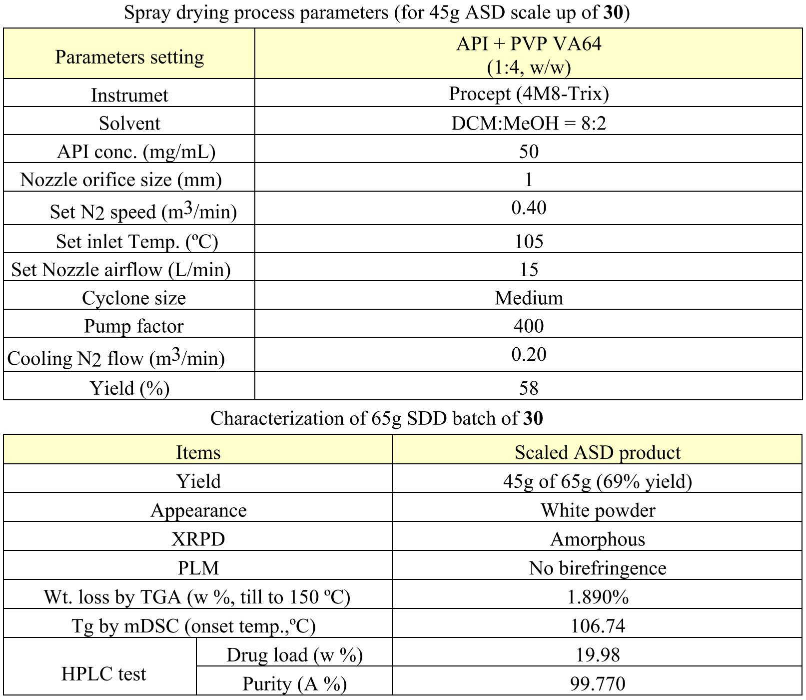

Spray drying process parameters (for 45g ASD scale up of **30**)

Parameters setting	API + PVP VA64 (1:4, w/w)
Instrumet	Procept (4M8-Trix)
Solvent	DCM:MeOH = 8:2
API conc. (mg/mL)	50
Nozzle orifice size (mm)	1
Set N2 speed (m^3/min)	0.40
Set inlet Temp. (ºC)	105
Set Nozzle airflow (L/min)	15
Cyclone size	Medium
Pump factor	400
Cooling N2 flow (m^3/min)	0.20
Yield (%)	58

Characterization of 65g SDD batch of **30**

Items		Scaled ASD product
Yield		45g of 65g (69% yield)
Appearance		White powder
XRPD		Amorphous
PLM		No birefringence
Wt. loss by TGA (w %, till to 150 ºC)		1.890%
Tg by mDSC (onset temp.,ºC)		106.74
HPLC test	Drug load (w %)	19.98
	Purity (A %)	99.770

Figure 16. Compound **30** spray-dry dispersion (SDD) process and characterization.

*pyrimidine-3-carboxamide, N-((1S,2S)-2-Methoxycyclobutyl)-7-(methylamino)-5-((2-oxo-2H-[1,2′-bipyridin]-3-yl)amino)pyrazolo-[1,5-a]pyrimidine-3-carboxamide (**ent-30**).* Isomers of **30** and **ent-30** (0.105 g) were separated into their pure enantiomers using chiral chromatography (CHIRAL PAK AD-H 250 × 4.6 mm, 5u) with 0.1% DEA_MEOH (70−30) to get pure fraction-a (FR-a) and fraction-b (FR-b). FR-a was concentrated under reduced pressure at 30 °C to afford pure FR-a as compound **30** (0.025 g). The absolute stereochemistry of compound **30** was assigned to be *R,R* based on the small molecule X-ray crystal structure and X-ray co-crystal structure of **30** with TYK2. MS(ES): *m/z* 461.42 $[M + H]^+$, LCMS purity: 99.70%, HPLC purity: 99.53%, CHIRAL HPLC purity: 100%, ^{1}H NMR (DMSO-d_6, 400 MHz): 9.05 (s, 1H), 8.27 (s, 1H), 8.37−8.35 (m, 2H), 8.23 (s, 1H), 8.12−8.05 (m, 1H), 7.97 (s, 1H), 7.88−7.87 (d, *J* = 8.0 Hz, 1H), 7.65−7.63 (d, *J* = 6.0 Hz, 1H), 7.58−7.56 (m, 1H), 6.48−6.45 (t, *J* = 6.8 Hz, 1H), 6.25 (s, 1H), 4.37−4.33 (m, 1H), 3.76−3.74 (d, *J* = 7.6 Hz, 1H), 3.23 (s, 3H), 2.93 (s, 3H), 2.82−2.79 (m, 2H), 2.16−2.08 (m, 2H).

FR-b was concentrated under reduced pressure at 30 °C to afford pure FR-b as compound **ent-30** (0.026 g). MS(ES): *m/z* 461.57 $[M + H]^+$, LCMS purity: 95.64%, HPLC purity: 95.06%, CHIRAL HPLC purity: 98.21%, ^{1}H NMR (DMSO-d_6, 400 MHz): 8.66−8.65 (d, *J* = 3.6 Hz, 1H), 8.38 (s, 1H), 8.34−8.32 (d, *J* = 5.6 Hz, 1H), 8.22 (s, 1H), 8.15−8.12 (d, *J* = 9.2 Hz, 1H), 8.08−8.04 (t, *J* = 8.0 Hz, 1H), 7.85−7.83 (d, *J* = 8.0 Hz, 1H), 7.63−7.61 (d, *J* = 7.2 Hz, 1H), 7.57−7.54 (m, 1H), 6.48−6.45 (t, *J* = 7.2 Hz, 1H), 6.19 (s, 1H), 4.35−4.31 (m, 1H), 3.76−3.71 (m, 2H), 3.21 (s, 3H), 2.92 (s, 3H), 2.82−2.79 (m, 2H), 2.17−2.06 (m, 2H).

The compound **30** spray-dry dispersion (SDD) process parameters and characterization are provided in Figure 16.

■ ASSOCIATED CONTENT

Supporting Information

The Supporting Information is available free of charge at https://pubs.acs.org/doi/10.1021/acs.jmedchem.3c00600.

PDB structure validation report for 8S98−**8** bound to TYK2 JH2 domain (PDF)

PDB structure validation report for 8S99−**11** bound to TYK2 JH2 domain (PDF)

PDB structure validation report for 8S9A−**30** bound to TYK2 JH2 domain (PDF)

PDB docking model of **30** bound to JAK1 JH2 domain used in Figure 10B,D (PDB)

Detailed experimental procedures and processes for the following are included: calculated properties, binding assays, kinase assays, kinase selectivity determinations, cellular assays, ADME assays, hERG and PDE4D inhibition assays, in vivo pharmacokinetic studies, in vivo PD and efficacy studies, synthetic scheme for compounds **7−9**, **12**, and **25**, synthetic scheme for compounds **10**, **11**, **13−16**, **19−24**, and **26−28**, synthetic scheme for compounds **17**, **18**, **29**, **30**, and **31−47**, synthetic procedures, analytical data for synthetic intermediates and final compounds, and HPLC traces for compounds evaluated in vivo. Additionally, data tables are provided for kinase selectivity for **11**, kinase selectivity for **30**, druglike/leadlike descriptor filters for the VS, crystallographic data, and model statistics; and histogram of FEP + predictions for a series of manuscript compounds (PDF)

Molecular formula strings together with some biochemical data; (CSV)

PDB IDs 8S98, 8S99, 8S9A, and CSD 2253269 have been deposited into their respective databases. The authors will release the atomic coordinates upon article publication.

■ AUTHOR INFORMATION

Corresponding Author

Scott D. Edmondson − *Nimbus Therapeutics, Boston, Massachusetts 02210, United States;* orcid.org/0000-0003-4865-2561; Email: scott.edmondson@nimbustx.com

Authors

Silvana Leit − *Nimbus Therapeutics, Boston, Massachusetts 02210, United States*

Downloaded from https://papernode.pages.dev

Jeremy Greenwood − *Schrödinger, Inc., New York, New York 10036, United States*
Samantha Carriero − *Nimbus Therapeutics, Boston, Massachusetts 02210, United States*
Sayan Mondal − *Schrödinger, Inc., New York, New York 10036, United States*
Robert Abel − *Schrödinger, Inc., New York, New York 10036, United States*
Mark Ashwell − *Nimbus Therapeutics, Boston, Massachusetts 02210, United States*
Heather Blanchette − *Nimbus Therapeutics, Boston, Massachusetts 02210, United States*
Nicholas A. Boyles − *Schrödinger, Inc., New York, New York 10036, United States*
Mark Cartwright − *Nimbus Therapeutics, Boston, Massachusetts 02210, United States*
Alan Collis − *Nimbus Therapeutics, Boston, Massachusetts 02210, United States*
Shulu Feng − *Schrödinger, Inc., New York, New York 10036, United States*
Phani Ghanakota − *Schrödinger, Inc., New York, New York 10036, United States;* orcid.org/0000-0002-2249-3681
Geraldine C. Harriman − *Nimbus Therapeutics, Boston, Massachusetts 02210, United States*
Vinayak Hosagrahara − *Nimbus Therapeutics, Boston, Massachusetts 02210, United States*
Neelu Kaila − *Nimbus Therapeutics, Boston, Massachusetts 02210, United States*
Rosanna Kapeller − *Nimbus Therapeutics, Boston, Massachusetts 02210, United States*
Salma B. Rafi − *Schrödinger, Inc., New York, New York 10036, United States*
Donna L. Romero − *Nimbus Therapeutics, Boston, Massachusetts 02210, United States*
Paul M. Tarantino − *Nimbus Therapeutics, Boston, Massachusetts 02210, United States*
Jignesh Timaniya − *Piramal Pharma Solutions, Ahmedabad 382215 Gujarat, India*
Angela V. Toms − *Nimbus Therapeutics, Boston, Massachusetts 02210, United States*
Ronald T. Wester − *Nimbus Therapeutics, Boston, Massachusetts 02210, United States*
William Westlin − *Nimbus Therapeutics, Boston, Massachusetts 02210, United States*
Bhaskar Srivastava − *Nimbus Therapeutics, Boston, Massachusetts 02210, United States*
Wenyan Miao − *Nimbus Therapeutics, Boston, Massachusetts 02210, United States*
Peter Tummino − *Nimbus Therapeutics, Boston, Massachusetts 02210, United States*
Joshua J. McElwee − *Nimbus Therapeutics, Boston, Massachusetts 02210, United States*
Craig E. Masse − *Nimbus Therapeutics, Boston, Massachusetts 02210, United States*

Complete contact information is available at:
https://pubs.acs.org/10.1021/acs.jmedchem.3c00600

Notes

The authors declare the following competing financial interest(s): SL, SC, MC, VH, NK, AVT, BS, PT, JJM, and SDE are employees of Nimbus Therapeutics and own equity in the company. SM, RA, SF, PG, and SR are employees of Schrödinger, Inc. and may own stock and/or stock options in that company.

ACKNOWLEDGMENTS

The authors would like to thank the Piramal Pharma Solutions team for the synthesis and spectroscopic characterization of analogs in this manuscript and Dr. Lewis Whitehead for logistical support with X-ray crystallography. We also thank Drs. Stuart Levy, Andrew Phimister, and Jon Lawson for CMC consulting support for advanced scale-ups and for the generation of the spray dry dispersion form of **30**. The research reported in this manuscript was funded by Nimbus Therapeutics, Boston, MA, and Schrödinger, Inc., New York, NY. This paper is dedicated to the memory of Dr. Jeremy R. Greenwood and Dr. William Westin, who are deceased.

ABBREVIATIONS

ADME, absorption distribution metabolism excretion;; BID, twice daily; Boc, *tert*-butyloxycarbonyl; CL_{pred}, predicted clearance; CXCL10, C−X−C motif chemokine ligand 10; CYP, cytochrome P450; ER, efflux ratio; FEP, free energy perturbation; hERG, human ether a go−go; IBD, inflammatory bowel disease; IFNα, interferon α; IFNγ, interferon γ; IVIVE, in vitro−in vivo extrapolation; JAK, Janus kinase; JH1, Janus homology 1; JH2, Janus homology 2; LoF, loss-of-function; MAE, mean absolute error; PBMC, peripheral blood mononuclear cell; PBPK, physiologically based pharmacokinetics; PD, pharmacodynamics; PK, pharmacokinetics; PPB, plasma protein binding; PXR, pregnane X receptor; QD, once daily; SAR, structure−activity relationships; SBDD, structure-based drug discovery; SDD, spray dry dispersion; SNP, single nucleotide polymorphism; TYK2, tyrosine kinase 2; VS, virtual screen; WB, whole blood

REFERENCES

(1) Gonciarz, M.; Pawlak-Bus, K.; Leszczynski, P.; Owczarek, W. TYK2 as a therapeutic target in the treatment of autoimmune and inflammatory diseases. *Immunotherapy* **2021**, *13*, 1135−1150.

(2) Zarrin, A. A.; Bao, K.; Lupardus, P.; Vucic, D. Kinase inhibition in autoimmunity and inflammation. *Nat. Rev. Drug Discovery* **2021**, *20*, 39−63.

(3) Ghoreschi, K.; Augustin, M.; Baraliakos, X.; Kronke, G.; Schneider, M.; Schreiber, S.; Schulze-Koops, H.; Zeißig, S.; Thaci, D. TYK2 inhibition and its potential in the treatment of chronic inflammatory immune diseases. *J. Dtsch. Dermatol. Ges.* **2021**, *19*, 1409−1420.

(4) Jostins, L.; Ripke, S.; Weersma, R. K.; Duerr, R. H.; McGovern, D. P.; Hui, K. Y.; Lee, J. C.; Philip Schumm, L.; Sharma, Y.; Anderson, C. A.; Essers, J.; Mitrovic, M.; Ning, K.; Cleynen, I.; Theatre, E.; Spain, S. L.; Raychaudhuri, S.; Goyette, P.; Wei, Z.; Abraham, C.; Achkar, J.-P.; Ahmad, T.; Amininejad, L.; Ananthakrishnan, A. N.; Andersen, V.; Andrews, J. M.; Baidoo, L.; Balschun, T.; Bampton, P. A.; Bitton, A.; Boucher, G.; Brand, S.; Buning, C.; Cohain, A.; Cichon, S.; D'Amato, M.; De Jong, D.; Devaney, K. L.; Dubinsky, M.; Edwards, C.; Ellinghaus, D.; Ferguson, L. R.; Franchimont, D.; Fransen, K.; Gearry, R.; Georges, M.; Gieger, C.; Glas, J.; Haritunians, T.; Hart, A.; Hawkey, C.; Hedl, M.; Hu, X.; Karlsen, T. H.; Kupcinskas, L.; Kugathasan, S.; Latiano, A.; Laukens, D.; Lawrance, I. C.; Lees, C. W.; Louis, E.; Mahy, G.; Mansfield, J.; Morgan, A. R.; Mowat, C.; Newman, W.; Palmieri, O.; Ponsioen, C. Y.; Potocnik, U.; Prescott, N. J.; Regueiro, M.; Rotter, J. I.; Russell, R. K.; Sanderson, J. D.; Sans, M.; Satsangi, J.; Schreiber, S.; Simms, L. A.; Sventoraityte, J.; Targan, S. R.; Taylor, K. D.; Tremelling, M.; Verspaget, H. W.; De Vos, M.; Wijmenga, C.; Wilson, D. C.; Winkelmann, J.; Xavier, R. J.; Zeissig, S.; Zhang, B.; Zhang, C. K.; Zhao, H.; Silverberg, M. S.; Annese, V.; Hakonarson, H.; Brant, S. R.;

Downloaded from https://papernode.pages.dev

Radford-Smith, G.; Mathew, C. G.; Rioux, J. D.; Schadt, E. E.; Daly, M. J.; Franke, A.; Parkes, M.; Vermeire, S.; Barrett, J. C.; Cho, J. H.; Cho, J. H.; International IBD Genetics Consortium. Host-microbe interactions have shaped the genetic architecture of inflammatory bowel disease. *Nature* **2012**, *491*, 119−124.

(5) Diogo, D.; Bastarache, L.; Liao, K. P.; Graham, R. R.; Fulton, R. S.; Greenberg, J. D.; Eyre, S.; Bowes, J.; Cui, J.; Lee, A.; Pappas, D. A.; Kremer, J. M.; Barton, A.; Coenen, M. J.; Franke, B.; Kiemeney, L. A.; Mariette, X.; Richard-Miceli, C.; Canhao, H.; Fonseca, J. E.; de Vries, N.; Tak, P. P.; Crusius, J. B.; Nurmohamed, M. T.; Kurreeman, F.; Mikuls, T. R.; Okada, Y.; Stahl, E. A.; Larson, D. E.; Deluca, T. L.; O'Laughlin, M.; Fronick, C. C.; Fulton, L. L.; Kosoy, R.; Ransom, M.; Bhangale, T. R.; Ortmann, W.; Cagan, A.; Gainer, V.; Karlson, E. W.; Kohane, I.; Murphy, S. N.; Martin, J.; Zhernakova, A.; Klareskog, L.; Padyukov, L.; Worthington, J.; Mardis, E. R.; Seldin, M. F.; Gregersen, P. K.; Behrens, T.; Raychaudhuri, S.; Denny, J. C.; Plenge, R. M. TYK2 Protein-Coding Variants Protect against Rheumatoid Arthritis and Autoimmunity, with No Evidence of Major Pleiotropic Effects on Non-Autoimmune Complex Traits. *PLoS One* **2015**, *10*, No. e0122271.

(6) Dendrou, C. A.; Cortes, A.; Shipman, L.; Evans, H. G.; Attfield, K. E.; Jostins, L.; Barber, T.; Kaur, G.; Kuttikkatte, S. B.; Leach, O. A.; Desel, C.; Faergeman, S. L.; Cheeseman, J.; Neville, M. J.; Sawcer, S.; Compston, A.; Johnson, A. R.; Everett, C.; Bell, J. I.; Karpe, F.; Ultsch, M.; Eigenbrot, C.; McVean, G.; Fugger, L. Resolving TYK2 locus genotype-to-phenotype differences in autoimmunity. *Sci. Transl. Med.* **2016**, *8*, 363ra149.

(7) Faezi, S. T.; Soltani, S.; Akbarian, M.; Aslani, S.; Hamzeh, E.; Jamshidi, A.; Ahmadzadeh, N.; Mahmoudi, M. Association of TYK2 rs34536443 polymorphism with Susceptibility to Systemic Lupus Erythematous in the Iranian Population. *Rheumatol. Res.* **2018**, *3*, 151−159.

(8) Couturier, N.; Bucciarelli, F.; Nurtdinov, R. N.; Debouverie, M.; Lebrun-Frenay, C.; Defer, G.; Moreau, T.; Confavreux, C.; Vukusic, S.; Cournu-Rebeix, I.; Goertsches, R. H.; Zettl, U. K.; Comabella, M.; Montalban, X.; Rieckmann, P.; Weber, F.; Muller-Myhsok, B.; Edan, G.; Fontaine, B.; Mars, L. T.; Saoudi, A.; Oksenberg, J. R.; Clanet, M.; Liblau, R. S.; Brassat, D. Tyrosine kinase 2 variant influences T lymphocyte polarization and multiple sclerosis susceptibility. *Brain* **2011**, *134*, 693−703.

(9) Li, Z.; Gakovic, M.; Ragimbeau, J.; Eloranta, M.-L.; Ronnblom, L.; Michel, F.; Pellegrini, S. Two rare disease-associated TYK2 variants are catalytically impaired but signaling competent. *J. Immunol.* **2013**, *190*, 2335−2344.

(10) Enerback, C.; Sandin, C.; Lambert, S.; Zawistowski, M.; Stuart, P. E.; Verma, D.; Tsoi, L. C.; Nair, R. P.; Johnston, A.; Elder, J. T. The psoriasis-protective TYK2 I684S variant impairs IL-12 stimulated pSTAT4 response in skin-homing CD4+ and CD8+ memory T-cells. *Nature* **2018**, *8*, 7043.

(11) Krueger, J. G.; McInnes, I. B.; Blauvelt, A. Tyrosine kinase 2 and Janus kinase−signal transducer and activator of transcription signaling and inhibition in plaque psoriasis. *J. Am. Acad. Dermatol.* **2022**, *86*, 148−157.

(12) Jo, C. E.; Gooderham, M.; Beecker, J. TYK2 inhibitors for the treatment of dermatologic conditions: the evolution of JAK inhibitors. *Int. J. Dermatol.* **2021**, *61*, 139−147.

(13) Hromadova, D.; Elewaut, D.; Inman, R. D.; Strobl, B.; Gracey, E. From science to success? Targeting tyrosine kinase 2 in spondyloarthritis and related chronic inflammatory diseases. *Front. Genet.* **2021**, *12*, 685280.

(14) Papp, K.; Gordon, K.; Thaci, D.; Morita, A.; Gooderham, M.; Foley, P.; Girgis, I. G.; Kundu, S.; Banerjee, S. Phase 2 Trial of Selective Tyrosine Kinase 2 Inhibition in Psoriasis. *N. Engl. J. Med.* **2018**, *379*, 1313−1321.

(15) Mease, P. J.; Deodhar, A. A.; van der Heijde, D.; Behrens, F.; Kivitz, A. J.; Neal, J.; Kim, J.; Singhal, S.; Nowak, M.; Banerjee, S. Efficacy and safety of selective TYK2 inhibitor, deucravacitinib, in a phase II trial in psoriatic arthritis. *Ann. Rheum. Dis.* **2022**, *81*, 815−822.

(16) Morand, E.; Pike, M.; Merrill, J. T.; Van Vollenhoven, R.; Werth, V. P.; Hobar, C.; Delev, N.; Shah, V.; Sharkey, B.; Wegman, T.; Catlett, I.; Banerjee, S.; Singhal, S. Efficacy and safety of deucravacitinib, and oral, selective, allosteric TYK2 inhibitor, in patients with active systemic lupus erythematosus: A Phase 2, randomized, double-blind, placebo-controlled study. *Ann. Rheum. Dis.* **2022**, *81*, 209 EULAR Abstract LB0004.

(17) He, X.; Chen, X.; Zhang, H.; Xie, T.; Ye, X.-Y. Selective TYK2 inhibitors as potential therapeutic agents: a patent review (2015−2018). *Expert Opin. Ther. Pat.* **2019**, *29*, 137−149.

(18) Zhang, C.; Qi, W.; Li, Y.; Tang, M.; Yang, T.; Liu, K.; Chen, Y.; Deng, D.; Xiang, M.; Chen, L. Discovery of 3-(4-(2-((1*H*-indol-5-yl)amino)-5-fluoropyrimidin-4-yl)-1*H*-pyrazol-1-1-yl)propanenitrile derivatives as selective TYK2 inhibitors for the treatment of inflammatory bowel disease. *J. Med. Chem.* **2021**, *64*, 1966−1988.

(19) Gonzalez Lopez de Turiso, F.; Guckian, K. Selective TYK2 inhibitors as potential therapeutic agents: a patent review (2019−2021). *Expert Opin. Ther. Pat.* **2022**, *32*, 365−379.

(20) Pardanani, A.; Laborde, R. R.; Lasho, T. L.; Finke, C.; Begna, K.; Al-Kali, A.; Hogan, W. J.; Litzow, M. R.; Leontovich, A.; Kowalski, M.; Tefferi, A. Safety and efficacy of CYT387, a JAK1 and JAK2 inhibitor, in myelofibrosis. *Leukemia* **2013**, *27*, 1322−1327.

(21) Mesa, R. A.; Cortes, J. Optimizing management of ruxolitinib in patients with myelofibrosis: the need for individualized dosing. *J. Hematol. Oncol.* **2013**, *6*, 79.

(22) Roda, G.; Dal Buono, A.; Argollo, M.; Danese, S. JAK selectivity: more precision less troubles. *Expert Rev. Gastroenterol. Hepatol.* **2020**, *14*, 789−796.

(23) Abel, R.; Mondal, S.; Masse, C.; Greenwood, J.; Harriman, G.; Ashwell, M. A.; Bhat, S.; Wester, R.; Frye, L.; Kapeller, R.; Friesner, R. A. Accelerating drug discovery through tight integration of expert molecular design and predictive scoring. *Curr. Opin. Struct. Biol.* **2017**, *43*, 38−44.

(24) Fensome, A.; Ambler, C. M.; Arnold, E.; Banker, M. E.; Brown, M. F.; Chrencik, J.; Clark, J. D.; Dowty, M. E.; Efremov, I. V.; Flick, A.; Gerstenberger, B. S.; Gopalsamy, A.; Hayward, M. M.; Hegen, M.; Hollingshead, B. D.; Jussif, J.; Knafels, J. D.; Limburg, D. C.; Lin, D.; Lin, T. H.; Pierce, B. S.; Saiah, E.; Sharma, R.; Symanowicz, P. T.; Telliez, J.-B.; Trujillo, J. I.; Vajdos, F. F.; Vincent, F.; Wan, Z.-K.; Xing, L.; Yang, X.; Yang, X.; Zhang, L. Dual inhibition of TYK2 and JAK1 for the treatment of autoimmune diseases: Discovery of ((S)-2,2-Difluorocyclopropyl)((1R,5S)-3-(2-((1-methyl-1H-pyrazol-4-yl)-amino)pyrimidin-4-yl)-3,8-diazabicyclo[3.2.1]octan-8-yl)methanone (PF-06700841). *J. Med. Chem.* **2018**, *61*, 8597−8612.

(25) Gerstenberger, B. S.; Ambler, C.; Arnold, E. P.; Banker, M.-E.; Brown, M. F.; Clark, J. D.; Dermenci, A.; Dowty, M. E.; Fensome, A.; Fish, S.; Hayward, M. M.; Hegen, M.; Hollingshead, B. D.; Knafels, J. D.; Lin, D. W.; Lin, T. H.; Owen, D. R.; Saiah, E.; Sharma, R.; Vajdos, F. F.; Xing, L.; Yang, X.; Yang, X.; Wright, S. W. Discovery of tyrosine kinase 2 (TYK2) inhibitor (PF-06826647) for the treatment of autoimmune diseases. *J. Med. Chem.* **2020**, *63*, 13561−13577.

(26) Leit, S.; Greenwood, J. R.; Mondal, S.; Carriero, S.; Dahlgren, M.; Harriman, G. C.; Kennedy-Smith, J. J.; Kapeller, R.; Lawson, J. P.; Romero, D. L.; Toms, A. V.; Shelley, M.; Wester, R. T.; Westlin, W.; McElwee, J. J.; Miao, W.; Edmondson, S. D.; Masse, C. E. Potent and selective TYK2-JH1 inhibitors highly efficacious in rodent model of psoriasis. *Bioorg. Med. Chem. Lett.* **2022**, *73*, 128891.

(27) Wrobleski, S. T.; Moslin, R.; Lin, S.; Zhang, Y.; Spergel, S.; Kempson, J.; Tokarski, J. S.; Strnad, J.; Zupa-Fernandez, A.; Cheng, L.; Shuster, D.; Gillooly, K.; Yang, X.; Heimrich, E.; McIntyre, K. W.; Chaudhry, C.; Khan, J.; Ruzanov, M.; Tredup, J.; Mulligan, D.; Xie, D.; Sun, H.; Huang, C.; D'Arienzo, C.; Aranibar, N.; Chiney, M.; Chimalakonda, A.; Pitts, W. J.; Lombardo, L.; Carter, P. H.; Burke, J. R.; Weinstein, D. S. Highly selective inhibition of tyrosine kinase 2 (TYK2) for the treatment of autoimmune diseases: Discovery of the allosteric inhibitor BMS-986165. *J. Med. Chem.* **2019**, *62*, 8973−8995.

(28) Liu, C.; Lin, J.; Langevine, C.; Smith, D.; Li, J.; Tokarski, J. S.; Khan, J.; Ruzanov, M.; Strnad, J.; Zupa-Fernandez, A.; Cheng, L.; Gillooly, K. M.; Shuster, D.; Zhang, Y.; Thankappan, A.; McIntyre, K. W.; Chaudhry, C.; Elzinga, P. A.; Chiney, M.; Chimalakonda, A.; Lombardo, L. J.; Macor, J. E.; Carter, P. H.; Burke, J. R.; Weinstein, D. S.

Downloaded from https://papernode.pages.dev

Discovery of BMS-986202: A clinical TYK2 inhibitor that binds to TYK2 JH2. *J. Med. Chem.* **2021**, *64*, 677−694.

(29) Moslin, R.; Gardner, D.; Santella, J.; Zhang, Y.; Duncia, J. V.; Liu, C.; Lin, J.; Tokarski, J. S.; Strnad, J.; Pedicord, D.; Chen, J.; Blat, Y.; Zupa-Fernandez, A.; Cheng, L.; Sun, H.; Chaudhry, C.; Huang, C.; D'Arienzo, C.; Sack, J. S.; Muckelbauer, J. K.; Chang, C.; Tredup, J.; Xie, D.; Aranibar, N.; Burke, J. R.; Carter, P. H.; Weinstein, D. S. Identification of imidazo[1,2-*b*]pyridazine TYK2 pseudokinase ligands as potent and selective allosteric inhibitors of TYK2 signalling. *MedChemComm* **2017**, *8*, 700−712.

(30) Tokarski, J. S.; Zupa-Fernandez, A.; Tredup, J. A.; Pike, K.; Chang, C. Y.; Xie, D.; Cheng, L.; Pedicord, D.; Muckelbauer, J.; Johnson, S. R.; Wu, S.; Edavettal, S. C.; Hong, Y.; Witmer, M. R.; Elkin, L. L.; Blat, Y.; Pitts, W. J.; Weinstein, D. S.; Burke, J. R. Tyrosine kinase 2-mediated signal transduction in T lymphocytes is blocked by pharmacological stabilization of its pseudokinase domain. *J. Biol. Chem.* **2015**, *290*, 11061−11074.

(31) Min, X.; Ungureanu, D.; Maxwell, S.; Hammaren, H.; Thibault, S.; Hillert, E.-K.; Ayres, M.; Greenfield, B.; Eksterowicz, J.; Gabel, C.; Walker, N.; Silvennoinen, O.; Wang, Z. Structural and functional characterization of the JH2 pseudokinase domain of JAK family tyrosine kinase 2 (TYK2). *J. Biol. Chem.* **2015**, *290*, 27261−27270.

(32) Lupardus, P. J.; Ultsch, M.; Wallweber, H.; Bir Kohli, P.; Johnson, A. R.; Eigenbrot, C. Structure of the pseudokinase−kinase domains from protein kinase TYK2 reveals a mechanism for Janus kinase (JAK) autoinhibition. *Proc. Natl. Acad. Sci. U.S.A.* **2014**, *111*, 8025−8030.

(33) Friesner, R. A.; Banks, J. L.; Murphy, R. B.; Halgren, T. A.; Klicic, J. J.; Mainz, D. T.; Repasky, M. P.; Knoll, E. H.; Shelley, M.; Perry, J. K.; Shaw, D. E.; Francis, P.; Shenkin, P. S. Glide: A new approach for rapid, accurate docking and scoring. 1. Method and assessment of docking accuracy. *J. Med. Chem.* **2004**, *47*, 1739−1749.

(34) Murphy, R. B.; Repasky, M. P.; Greenwood, J. R.; Tubert-Brohman, I.; Jerome, S.; Annabhimoju, R.; Boyles, N. A.; Schmitz, C. D.; Abel, R.; Farid, R.; Friesner, R. A. WScore: A flexible and accurate treatment of explicit water molecules in ligand-receptor docking. *J. Med. Chem.* **2016**, *59*, 4364−4384.

(35) Wang, L.; Wu, Y.; Deng, Y.; Kim, B.; Pierce, L.; Krilov, G.; Lupyan, D.; Robinson, S.; Dahlgren, M. K.; Greenwood, J.; Romero, D. L.; Masse, C.; Knight, J. L.; Steinbrecher, T.; Beuming, T.; Damm, W.; Harder, E.; Sherman, W.; Brewer, M.; Wester, R.; Murcko, M.; Frye, L.; Farid, R.; Lin, T.; Mobley, D. L.; Jorgensen, W. L.; Berne, B. J.; Friesner, R. A.; Abel, R. Accurate and reliable prediction of relative ligand binding potency in prospective drug discovery by way of a modern free-energy calculation protocol and force field. *J. Am. Chem. Soc.* **2015**, *137*, 2695−2703.

(36) For a more extensive assessment of the SAR of the pyrazolopyrimidine pyridone series, see Masse, C. E.; Greenwood, J. R.; Mondal, S.; Cowen, S. D.; Mclean, T. H. TYK2 inhibitors and uses thereof. WO 2019 023468 A1, 2019.

(37) Liu, C.; Lin, J.; Moslin, R.; Tokarski, J. S.; Muckelbauer, J.; Chang, C. Y.; Tredup, J.; Xie, D.; Park, H.; Li, P.; Wu, D.-R.; Strnad, J.; Zupa-Fernandez, A.; Cheng, L.; Chaudhry, C.; Chen, J.; Chen, C.; Sun, H.; Elzinga, P.; D'Arienzo, C.; Gillooly, K.; Taylor, T. L.; McIntyre, K. W.; Salter-Cid, L.; Lombardo, L. J.; Carter, P. H.; Aranibar, N.; Burke, J. R.; Weinstein, D. S. Identification of Imidazo[1.2-*b*]pyridazine Derivatives as Potent, Selective, and Orally Active Tyk2 JH2 Inhibitors. *ACS Med. Chem. Lett.* **2019**, *10*, 383−388.

(38) Liu, Y.; Holdbrooks, A. T.; De Sarno, P.; Rowse, A. L.; Yanagisawa, L. L.; McFarland, B. C.; Harrington, L. E.; Raman, C.; Sabbaj, S.; Benveniste, E. N.; Qin, H. Therapeutic Efficacy of Suppressing the JAK/STAT Pathway in Multiple Models of Experimental Autoimmune Encephalomyelitis. *J. Immunol.* **2014**, *192*, 59−72.

(39) Burke, J. R.; Cheng, L.; Gillooly, K. M.; Strnad, J.; Zupa-Fernandez, A.; Catlett, I. M.; Zhang, Y.; Heimrich, E. M.; McIntyre, K. W.; Cunningham, M. D.; Carman, J. A.; Zhou, X.; Banas, D.; Chaudhry, C.; Li, S.; D'Arienzo, C.; Chimalakonda, A.; Yang, X.; Xie, J. H.; Pang, J.; Zhao, Q.; Rose, S. M.; Huang, J.; Moslin, R. M.; Wrobleski, S. T.; Weinstein, D. S.; Salter-Cid, L. M. Autoimmune pathways in mice and humans are blocked by pharmacological stabilization of the TYK2 pseudokinase domain. *Sci. Transl. Med.* **2019**, *11*, No. eaaw1736.

(40) Ghose, A. K.; Viswanadhan, V. N.; Wendoloski, J. J. Prediction of Hydrophobic (Lipophilic) Properties of Small Organic Molecules Using Fragmental Methods: An Analysis of ALOGP and CLOGP Methods. *J. Phys. Chem. A* **1998**, *102*, 3762−3772.

(41) Leung, S. S. F.; Sindhikara, D.; Jacobson, M. P. Simple predictive models of passive membrane permeability incorporating size-dependent membrane-water partition. *J. Chem. Inf. Model.* **2016**, *56*, 924−929.

(42) Mondal, S.; Tresadern, G.; Greenwood, J.; Kim, B.; Kaus, J.; Wirtala, M.; Steinbrecher, T.; Wang, L.; Masse, C.; Farid, R.; Abel, R. A Free Energy Perturbation Approach to Estimate the Intrinsic Solubilities of Drug-like Small Molecules. *ChemRxiv* **2019**, DOI: 10.26434/chemrxiv.10263077.v1. Cambridge: Cambridge Open Engage

(43) Ishizaki, M.; Muromoto, R.; Akimoto, T.; Sekine, Y.; Kon, S.; Diwan, M.; Maeda, H.; Togi, S.; Shimoda, K.; Oritani, K.; Matsuda, T. Tyk2 is a therapeutic target for psoriasis-like skin inflammation. *Int. Immunol.* **2014**, *26*, 257−267.

(44) Wajima, T.; Fukumura, K.; Yano, Y.; Oguma, T. Prediction of human clearance from animal data and molecular structural parameters using multivariate regression analysis. *J. Pharm. Sci.* **2002**, *91*, 2489−2499.

(45) Zou, P.; Yu, Y.; Zheng, N.; Yang, Y.; Paholak, H. J.; Yu, L. X.; Sun, D. Applications of Human Pharmacokinetic Prediction in First-in-Human Dose Estimation. *AAPS J.* **2012**, *14*, 262−281.

(46) Toms, A. V.; Deshpande, A.; McNally, R.; Jeong, Y.; Rogers, J. M.; Kim, C. U.; Gruner, S. M.; Ficarro, S. B.; Marto, J. A.; Sattler, M.; Griffin, J. D.; Eck, M. J. Structure of a pseudokinase domain switch that controls oncogenic activation of Jak kinases. *Nat. Struct. Mol. Biol.* **2013**, *20*, 1221−1223.

(47) Newton, A. S.; Deiana, L.; Puleo, D. E.; Cisneros, J. A.; Cutrona, K. J.; Schlessinger, J.; Jorgensen, W. L. JAK2 JH2 fluorescence polarization assay and crystal structures for complexes with three small molecules. *ACS Med. Chem. Lett.* **2017**, *8*, 614−617.

(48) Some reagents used in the rat PD model are described in Mikus Mikus, L. D.; Rosenthal, L. A.; Sorkness, R. L.; Lemanski, R. F.; Lemanske, R. F. Reduced Interferon- γ Secretion by Natural Killer Cells from Rats Susceptible to Postviral Chronic Airway Dysfunction. *Am. J. Respir. Cell Mol. Biol.* **2001**, *24*, 74−82.

(49) Some reagents used in the rat PD model are described in Sun, B.; Li, H.-L.; Wang, J.-H.; Wang, G.-Y.; Zhao, R.; Mu, L.-L.; Jin, L.-H. Passive transfer of experimental autoimmune neuritis by IL-12 and IL-18 synergistically potentiated lymphoid cells is regulated by NKR-P1+ cells. *Scand. J. Immunol.* **2007**, *65*, 412−420.

(50) Hegen, M.; Keith, J. C., Jr; Collins, M.; Nickerson-Nutter, C. L. Utility of animal models for identification of potential therapeutics for rheumatoid arthritis. *Ann. Rheum. Dis.* **2008**, *67*, 1505−1515.

(51) Mizoguchi, E.; Low, D.; Ezaki, Y.; Okada, T. Recent updates on the basic mechanisms and pathogenesis of inflammatory bowel diseases in experimental animal models. *Intest. Res.* **2020**, *18*, 151−167.

(52) Witschel, M. C.; Hoffken, H. W.; Seet, M.; Parra, L.; Mietzner, T.; Thater, F.; Niggeweg, R.; Rohl, F.; Illarionov, B.; Rohdich, F.; Kaiser, J.; Fischer, M.; Bacher, A.; Diederich, F. Inhibitors of the herbicidal target IspD: Allosteric site binding. *Angew. Chem., Int. Ed.* **2011**, *50*, 7931−7935.

(53) Zhou, Y.; Li, X.; Shen, R.; Wang, X.; Zhang, F.; Liu, S.; Li, D.; Liu, J.; Li, P.; Yan, Y.; Dong, P.; Zhang, Z.; Wu, H.; Zhuang, L.; Chowdhury, R.; Miller, M.; Issa, M.; Mao, Y.; Chen, H.; Feng, J.; Li, J.; Bai, C.; He, F.; Tao, W. Novel small molecule tyrosine kinase 2 pseudokinase ligands block cytokine-induced TYK2-mediated signaling pathways. *Front. Immunol.* **2022**, *13*, 884399.

(54) Locke, G. A.; Muckelbauer, J.; Tokarski, J. S.; Barbieri, C. M.; Belic, S.; Falk, B.; Tredup, J.; Wang, Y.-K. Identification and characterization of TYK2 pseudokinase domain stabilizers that allosterically inhibit TYK2 signaling. *Methods Enzymol.* **2022**, *667*, 685−727.

Downloaded from https://papernode.pages.dev

NOTE ADDED AFTER ASAP PUBLICATION

After this paper was published ASAP July 10, 2023, corrections were made to the abstract graphic and Table 5. The corrected version was reposted July 10, 2023. A correction was also made to Figure 13B, and the corrected version reposted July 20, 2023.


CAS BIOFINDER DISCOVERY PLATFORM™
ELIMINATE DATA SILOS. FIND WHAT YOU NEED, WHEN YOU NEED IT.
A single platform for relevant, high-quality biological and toxicology research
Streamline your R&D
CAS
A division of the American Chemical Society

Downloaded from https://papernode.pages.dev